

Through the Lens of a Momentum Microscope: Viewing Light-Induced Quantum Phenomena in 2D Materials

Ouri Karni, Iliya Esin, and Keshav M. Dani*

Van der Waals (vdW) materials at their 2D limit are diverse, flexible, and unique laboratories to study fundamental quantum phenomena and their future applications. Their novel properties rely on their pronounced Coulomb interactions, variety of crystal symmetries and spin-physics, and the ease of incorporation of different vdW materials to form sophisticated heterostructures. In particular, the excited state properties of many 2D semiconductors and semi-metals are relevant for their technological applications, particularly those that can be induced by light. In this paper, the recent advances made in studying out-of-equilibrium, light-induced, phenomena in these materials are reviewed using powerful, surface-sensitive, time-resolved photoemission-based techniques, with a particular emphasis on the emerging multi-dimensional photoemission spectroscopy technique of time-resolved momentum microscopy. The advances this technique has enabled in studying the nature and dynamics of occupied excited states in these materials are discussed. Then, the future research directions opened by these scientific and instrumental advancements are projected for studying the physics of 2D materials and the opportunities to engineer their band-structure and band-topology by laser fields.

1. Introduction

The last two decades have witnessed an explosion of research on van-der-Waals (vdW) materials—a wide class of solids in which planar crystal sheets are bonded together by vdW forces. Typically, these materials can be thinned down to just a few atomic layers, or even to a single atomic sheet, thereby realizing two-dimensional (2D) variants of their traditional bulk forms. Since the first exfoliation of a monolayer (1L) of graphene in the early 2000's, a variety of vdW materials have been isolated and studied in their 2D limit including metals, wide-gap insulators, semiconductors, semi-metals, superconductors, magnetic materials, and more.^[1] Among these, semi-metals, like graphene, and the class of 2D semiconductors, often represented by the group VI transition-metal dichalcogenides (TMDC), have created exciting new opportunities in fundamental condensed matter physics, as

well as applications in electronic, optoelectronic, and quantum technologies.^[2–4] Due to the dramatic changes in optical interaction and band-structure that can occur in transitioning from the few-layer to 1L limit, 2D semiconductors and semi-metals provide unique opportunities in 2D light-matter interactions and ultrathin optoelectronic devices. This merits the exploration of their light-induced physics leading to novel out-of-equilibrium quantum phenomena.

One of the key properties of 2D materials is the enhanced electron–electron Coulomb interactions arising from their reduced dielectric screening and low dimensionality. These interactions strongly modify not just the equilibrium band-structure, but more so the (photo)excited band-structure.^[5] For example, strongly bound excitons^[6]—excited states composed of bound electrons and holes—dominate the optical response of 2D semiconductors, even at room temperature. These excitons display a rich variety of species with different spins,^[7] momenta,^[8] and charge,^[9] impacting the spectrum, dynamics, and applications of their light–matter interaction.

Another property of 2D materials is their ability to stack onto other 2D materials and substrates with almost no constraints.^[10] The interlayer interactions in these structures facilitate a unique means for engineering the heterostructure properties and functionality beyond those of the constituent materials.^[11,12] These properties include the momentum-dependent interlayer

O. Karni
Department of Applied Physics
Stanford University
Stanford, CA 94305, USA

O. Karni
SLAC National Accelerator Laboratory
Menlo Park, CA 94025, USA

I. Esin
Department of Physics
California Institute of Technology
Pasadena, CA 91125, USA

K. M. Dani
Femtosecond Spectroscopy Unit
Okinawa Institute of Science and Technology Graduate University
Onna-son, Okinawa 904-0495, Japan
E-mail: kmdani@oist.jp

 The ORCID identification number(s) for the author(s) of this article can be found under <https://doi.org/10.1002/adma.202204120>.

© 2022 The Authors. Advanced Materials published by Wiley-VCH GmbH. This is an open access article under the terms of the Creative Commons Attribution-NonCommercial License, which permits use, distribution and reproduction in any medium, provided the original work is properly cited and is not used for commercial purposes.

DOI: 10.1002/adma.202204120

hybridization of electronic orbitals comprising the Bloch-states,^[13,14] dielectric influence on the excitonic spectrum of each layer,^[15] and, in the case of 2D semiconductors, the emergence of excitonic states that are distributed between the layers, namely, interlayer excitons (ILX).^[16] Furthermore, small mismatches in the lattice constant or orientation between two lattices stacked together lead to the formation of a moiré pattern—a superlattice structure emerging from the periodic offsets between the atomic positions of the two adjacent layers. These moiré patterns effectively create a spatial modulation of electronic and excitonic energies resulting in arrays of potential wells that can host single-photon emitters.^[17] Complementarily, the moiré superlattices are manifested in momentum-space in the folding of electronic and excitonic bands of the constituent materials into mini-bands.^[18–20] These mini-bands have highly tunable dispersion relations, and under certain conditions can even become flat. The flat-band limit of the moiré superlattices exhibits various exotic phenomena such as correlated electronic phases in twisted bilayers and trilayers of graphene,^[21–24] as well as semiconducting hetero- and homobilayers.^[25–27] Moiré superlattices have been predicted to support non-trivial topologies of the ILX bandstructure^[17,18,28–30] and to simulate Hubbard model physics.^[18,20]

Finally, the 2D TMDC semiconductors exhibit broken inversion symmetry and strong spin-orbit coupling, which are essential for technological applications such as valleytronics,^[31] and for inducing emergent topological phenomena, such as the quantum spin Hall effect.^[32] Moreover, even in the absence of broken inversion symmetry or strong spin-orbit coupling in materials like graphene, topological phenomena can be externally induced by subjecting the material to a time-periodic electromagnetic field. This approach, known as ‘Floquet band engineering’ allows to design the bandstructure and topological properties of a material ‘on demand’ by external periodic driving.

To study these and other novel properties, 2D materials have been probed using a variety of experimental techniques. Among these techniques, angle-resolved photoemission spectroscopy (ARPES) has been particularly successful in probing the impact of the above-mentioned enhanced Coulomb interactions, unique interfaces in stacked heterostructures, spin-valley, and topological physics of these materials. A major reason for the success of such photoemission techniques is that their “surface only” sensitivity is a perfect match for the “all surface” nature of 2D materials. Over time, powerful variants of the ARPES technique, such as micron-scale ARPES (μ ARPES), spin-resolved ARPES (SR-ARPES), and time-resolved ARPES (TR-ARPES), also began providing powerful insights into the ground- and excited state physics of 2D materials and their heterostructures. Recently, the emergence of time-resolved momentum microscopy^[33]—a multi-dimensional photoemission spectroscopy platform with the potential to resolve photoemitted electrons simultaneously in space, time, momentum, energy, and spin, has promised a new era in studying light-induced, out-of-equilibrium, quantum phenomena and applications in 2D semiconductors. On top of efficiently combining the capabilities of all of the above ARPES variants, time-resolved momentum-microscopy techniques offer a 2D view of momentum-space that can be invaluable in understanding certain phenomena.

In this paper, we review the developments in ARPES and multi-dimensional momentum microscopy instrumentation and the scientific breakthroughs it has been supporting, including a projection toward the future explorations of quantum effects in 2D materials. We structure this review as follows. In Section 2, we survey the instrumentation, and associated developments in the field. Therein, we first briefly review the concept of band-structure characterization using the classical ARPES technique, and its capabilities and limitations when applied to the exploration of 2D materials. We then introduce the ARPES variants: μ ARPES, SR-ARPES, and TR-ARPES, including their unique virtues and constraints. Finally, we introduce the emerging platform of momentum microscopy and show how it can serve as an efficient tool to perform multi-dimensional photoemission spectroscopy.

In Section 3, we discuss the progress in investigating photo-excited states in 2D semiconductors. We begin from the independent quasiparticle picture and continue to discuss two-body excitons. Then, we outline the directions for future study of other many-body phenomena. In the following Section 4, we move to the light-induced manipulation of the bandstructures using Floquet-engineering. Our main focus in this section is inducing topological phenomena by circularly polarized lasers. Throughout, we emphasize the opportunities that have been laid by multi-dimensional momentum-microscopy. We end the discussion with a brief outlook on the instrumental progress needed to support such research directions, in Section 5.

2. Advances in Instrumentation

2.1. Angle-Resolved Photoemission Spectroscopy

2.1.1. Measurement Concept

ARPES is a powerful technique that over the recent decades has been providing valuable information about the electronic band dispersions in a crystal and their interactions therein.

In a basic ARPES measurement,^[34] the sample is irradiated by high-energy photons, which then photoemit electrons from the sample based on the photoelectric effect. The kinetic energy (E_{kin}) of the photoemitted electron, and the angle θ at which it is emitted from the sample surface (Figure 1a), provide direct information about the electron’s energy (E) and lateral momentum (k_{\parallel}) in the sample:

$$E_{\text{kin}} = h\nu - \Phi + E \quad (1)$$

$$k_{\parallel}^f = k_{\parallel} \quad (2)$$

$$\hbar k_{\parallel}^f = \sqrt{2m_0 E_{\text{kin}}} \sin(\theta) \quad (3)$$

where Φ is the workfunction of the material, $h\nu$ is the photon energy, m_0 is the mass of the free electron in vacuum, and E is the energy of the electron in the sample measured with respect to the Fermi level ($E < 0$ denotes states below the Fermi energy). The lateral momentum of the photoelectron, k_{\parallel}^f , is conserved in the photoemission process (Equation (2)), allowing its

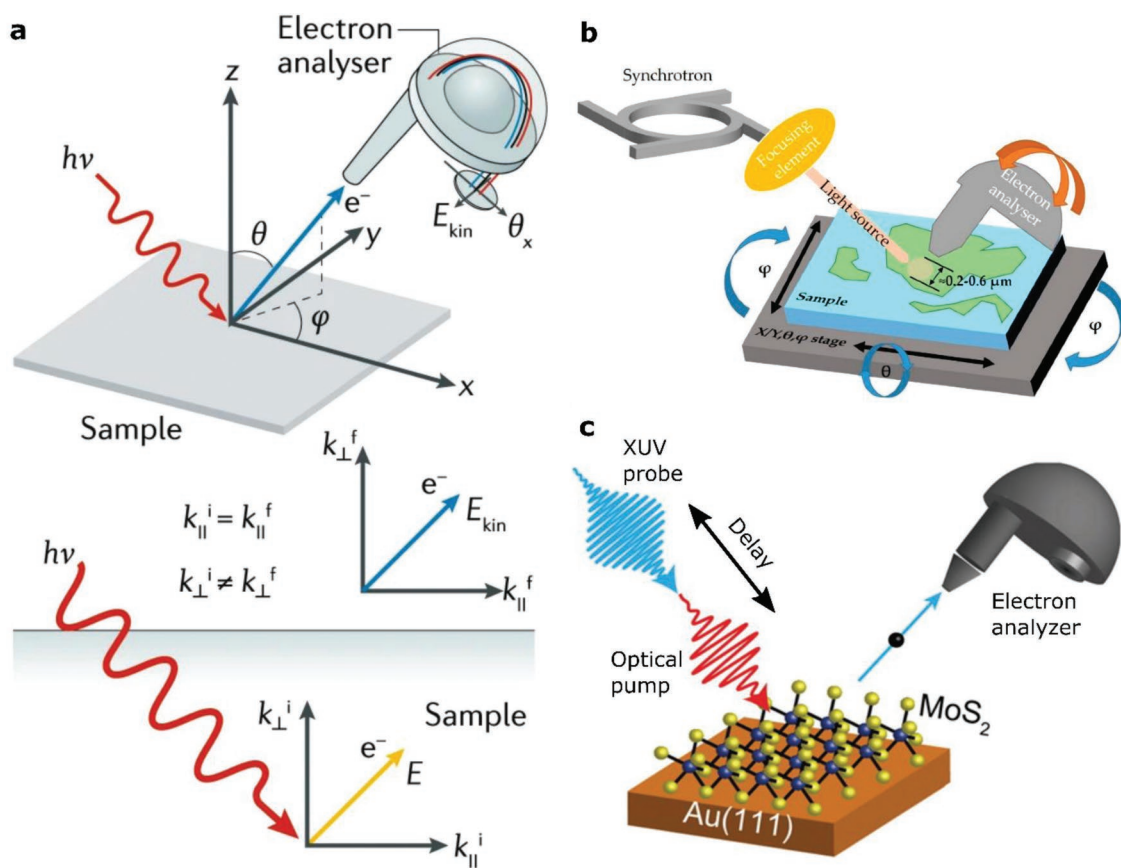


Figure 1. ARPES concept and its variants. a) The static ARPES concept. The photoemission pulse ejects electrons off the sample. These are collected and detected using a hemispherical analyzer measuring their kinetic energy, E_{kin} , and photoemission angle, θ . The conservation of energy and lateral momentum in the photoemission process (Equations (1)–(3)), enables to deduce the electronic band dispersions, $E(k_{||})$, in the sample itself. Reproduced with permission.^[35] Copyright 2019, Nature Publishing Group. b) The concept of μ ARPES. The photoemitting light is focused on a small region of the sample. The focusing of ultra-violet (UV) and X-ray light results in significant signal losses, requiring an intense light source, typically available in synchrotron facilities. Reproduced under the terms of the CC BY Creative Commons Attribution 4.0 International license.^[36] Copyright 2018, The authors, published by MDPI Journals. c) The concept of TR-ARPES. The sample (1L MoS₂ on a gold substrate, in this case) is first excited by an optical pulse, and the photoemitting probe pulse follows at a controlled delay, to probe the excited band-structure. Reproduced with permission.^[37] Copyright 2015, ACS Publications.

mapping to the photoemission angle via the free electron dispersion relation (Equation (3)). In the case of three dimensional (3D) bulk samples, one can also obtain the momentum perpendicular to the sample surface, under additional constraints and measurements.^[34]

2.1.2. Typical ARPES Setup

The measurement of E_{kin} and θ of the photoelectrons is influenced by two central parts of an ARPES setup: the photon source and the energy analyzer.

Photon Source: Typically, ARPES experiments utilize photons in the energy range of a few eV to a few hundred eV. At the lower end of the photon energy, one needs to at least overcome the workfunction of materials, which tend to be in the 4–6 eV range. The photoemission horizon, or cutoff

$$0 \leq \hbar^2 k_{||}^2 / 2m_0 \leq \hbar\nu - \Phi + E \quad (4)$$

directly obtained from Equations (1)–(3), dictates that higher photon energies (several tens of eV) are needed to photoemit valence electrons from the edges of the Brillouin Zone (BZ) of most materials (large $k_{||}$), or from deep below the Fermi level (large $|E|$, with $E < 0$). Even higher levels of photon energy, in the hundreds of eV range, allow one to perform core level spectroscopy,^[38,39] or to map the atomic orbitals that comprise the bands.^[40] In addition, the spectral bandwidth of the photon source, its polarization state, and frequency tunability, are also important to an ARPES measurement. They offer the ability to obtain high energy resolution, to compensate for the matrix elements that determine the efficiency of the photoemission process,^[41] and to access the component of momentum perpendicular to the surface in the study of bulk materials, respectively.^[42]

Typically, four different kinds of light sources have been utilized in ARPES measurements.^[34] Synchrotrons are the most ubiquitous, providing a high flux, tunability, reasonably narrow bandwidths, and some polarization control. Gas discharge lamps are another common alternative that provides photons in

the few tens of eV with frequency bandwidths around 1 meV, yet without polarization control. Table-top laser-based sources can cover the low end of the energy scale (6–40 eV) using nonlinear optical techniques. They can provide full polarization control, as well as narrow linewidths at the low end of the photon energy range.^[43,44] However, table-top laser-based sources lack brightness compared to the other types of light sources, particularly at higher photon energies. In contrast, they easily provide the possibility of femtosecond temporal resolution, which makes them very useful to the time-resolved techniques discussed below. Finally, free electron lasers (FELs)^[45] also act as very attractive light sources for ARPES measurements, wherein one could also obtain femtosecond time-resolution along with the other advantages of synchrotron radiation, such as high flux and tunability in the soft-X-ray spectral domain. These energies (>100 eV) are necessary to reach photoemission horizons that encompass the entire momentum-support of atomic orbitals^[40] in solids. As well, they offer photoemission from core-levels that may shed light on the dynamics of valence excitations in the material.^[39,46] Thus, experiments conducted in FEL facilities have the potential for mapping electronic populations with atomic resolutions. Nonetheless, the high flux and timing structure of these pulses can result in substantial space-charge effects.^[47]

Analyzer: The second central component of an ARPES setup is the energy analyzer, which is used to resolve the kinetic energy of the photoemitted electrons. The most common type of energy analyzer is the hemispherical analyzer (HA), which consists of two concentric metallic hemispheres at different voltages. Having chosen a particular high-symmetry line of the BZ of a material, electrons with different k_{\parallel} along that line are mapped onto the entrance slit of the HA. These electrons then follow a curved trajectory between the two hemispheres, such that electrons of different energy are dispersed in a direction perpendicular to the entrance slit. A 2D camera at the exit slit of the HA then records k_{\parallel} along one axis and E_{kin} along the other axis (see Figure 1a). By appropriately tilting and reorienting the sample, one can map out the energy-momentum dispersion along other high-symmetry axes of the BZ. The energy and momentum resolutions of this measurement are primarily determined by the widths of the entrance and exit slits, along with the pixel size of the detector. To date, the HA offers some of the best energy and momentum resolutions available.

Recently, another type of energy analyzers has also been developed, known as the time-of-flight (ToF) analyzers.^[48] These energy analyzers have the potential to offer higher throughput and faster data acquisition, and are well suited for MM, as further discussed in Section 2.3.

2.1.3. ARPES and 2D Materials

Due to the relatively small escape depths of photoemitted electrons from the sample, ARPES is essentially a surface-sensitive technique. This surface sensitivity creates some challenges while attempting to study bulk materials.^[49] Alternatively, one can restrict oneself to studying just the surface states of a material, which leaves one with incomplete knowledge about its full electronic structure. In contrast, 2D materials are perfectly suited to the ARPES technique. The absence of the third

dimension means that ARPES can provide rich and “complete” information about the material.

Nonetheless, despite this well-suited marriage between a “surface only” technique and an “all surface” class of materials, the union, like most well-suited unions, presents its own set of challenges. Most of the interesting physics for 2D materials happens at the edges of the BZ. For UV photons, these states lie outside the photoemission horizon due to their large k_{\parallel} (Equation (4)). Instead, extreme UV (XUV) photons with energies of ≈ 20 eV or larger are required. This eliminates the possibility to use the more common UV-based table-top systems and has required one to rely on synchrotron sources for high-quality measurements.

Furthermore, the unique properties of 2D TMDCs outlined earlier—novel heterostructures, unique spin physics, and excited state properties require certain enhancements to the standard ARPES capabilities. In the next sub-section, we describe the variants of the ARPES technique that aim to access these unique properties.

2.2. ARPES Variants

2.2.1. Spatially Resolved ARPES

2D material samples made by the standard techniques of mechanical exfoliation or chemical vapor deposition (CVD) growth tend to have only micron-scale regions with reasonable sample homogeneity, such as single-crystalline domains, uniform thickness, and dielectric environments. Heterostructures of 2D materials that are made by overlapping such homogeneous regions are then even smaller in size. Since traditional ARPES measurements have spot sizes that range in the few hundred microns to mm range, one ends up integrating signals with large inhomogeneity, from multiple crystalline domains, and also background regions of the sample that do not contain the same number of layers. These issues are discussed in more detail in the specific context of measuring excitonic states in Section 3.3.2. In order to overcome these challenges, one needs to perform ARPES with a micron-scale resolution, dubbed μ ARPES.

The most successful approach for μ ARPES studies of 2D materials thus far has involved the tight focusing of XUV beams using specialized focusing elements in the XUV^[36] (Figure 1b). Although these focusing elements tend to be very lossy, particularly for smaller spot sizes, the high flux generated by synchrotrons can offset these losses. Currently, four specialized synchrotron beamlines around the world—Antares at Soleil in France, I05 at Diamond in the UK, Maestro at the ALS in the US, and the Spectromicroscopy beamline at Elettra in Italy^[36]—have successfully implemented the bulk of μ ARPES measurements reported in the literature, with spatial resolutions going down to sub-microns.^[36] Nonetheless, access to these specialized synchrotron beamlines remains a limiting factor.

2.2.2. SR-ARPES

As described previously, strong spin-orbit coupling and the lack of inversion symmetry in TMDCs lead to a unique valley-spin

locking. The spin texture in these materials is also intimately related to the topology of their band-structure. Thus, measuring the spin state of the photoemitted electron is critical in valleytronic and Floquet engineering applications. This requires SR-ARPES.

While some SR-ARPES measurements on 2D materials have been strikingly successful,^[50] SR-APRES remains a very challenging experiment and has generally suffered from low detection efficiency. Conventional instrumentation resolves the spin of only one energy and momentum channel at a time, substantially reducing the throughput of the experiments.^[51] Recently, multi-channel spin-resolving techniques have emerged that can substantially improve the efficiency of spin detection. These spin-resolving techniques are well suited to the multi-channel detection techniques of ToF MM as discussed further below.^[33]

2.2.3. TR-ARPES

Finally, light-induced phenomena are of fundamental and technological importance in 2D materials, ranging from the study of photoexcited states to Floquet engineering, as mentioned previously. For such studies, the timescale of photoexcited dynamics and the need for intense light fields necessitate the use of femtosecond light pulses and TR-ARPES measurements.

The basic idea of femtosecond TR-ARPES measurements is to utilize the stroboscopic pump-probe technique. Here, a femtosecond pump pulse first excites the sample and is then followed by a time-delayed femtosecond probe pulse that performs the ARPES measurement described in Section 2.1.1 (as illustrated in Figure 1c). By assembling the ARPES spectra collected at different delays, one obtains a “movie” of the dynamics after photoexcitation.

Of the ARPES-useful light sources discussed in Section 2.1.2, table-top sources offer the most reliable, repeatable, and easily maneuvered femtosecond pulses. Yet, the need for XUV photons to access the edges of the BZ in 2D materials makes this a challenging experiment for table-top sources. While table-top TR-ARPES setups can utilize higher harmonic generation (HHG) techniques to generate femtosecond pulses in the XUV, the flux is usually quite low. Moreover, the need for high-flux, low repetition rate (kHz) lasers to implement HHG techniques also results in low throughput, and in space charge effects.^[52] Recent developments in HHG with table-top sources have begun to realize high flux XUV generation into the MHz regime,^[53–55] which is a promising development for TR-ARPES.

Even though these different variants of ARPES have independently provided interesting knowledge about 2D materials, it is clear that their individual capabilities need to be combined to access and study the true potential of 2D materials. For example, given sample size considerations of heterostructures, both SR-ARPES and TR-ARPES also require micron-scale spatial resolutions. Moreover, given the general importance of spin to the photoexcited states, one would expect to gain by combining aspects of time- and spin-resolved photoemission techniques as well. However, combining all the above experimental techniques of time-, spin-, and spatially-resolved ARPES is not practical. To begin with, the synchrotron sources that are capable of micron-scale resolution are not designed for femtosecond-scale

temporal resolution. On the other hand, table-top sources of XUV light, which easily provide femtosecond-scale resolutions, have barely been able to provide the required flux, and have not been able to focus the XUV light to a few microns spot size. Adding inefficient spin-resolution schemes to these experiments makes the measurements increasingly complex. Nonetheless, multidimensional photoemission spectroscopy remains a highly sought-after goal.^[36]

In recent years, alternate attempts to efficiently perform time-, space-, spin-, and angle-resolved photoemission spectroscopy have led to the development of a substantially different experimental platform called MM. We describe this emerging technique next.

2.3. Momentum Microscopy

MM is a type of cathode lens or immersion lens microscopy. In this technique, the sample forms a part of the imaging system, by applying various shapes of electrostatic fields between it and the objective lens. This supports various lens modes, such as the standard extractor mode (with positive anode voltage), the zero-field mode (advantageous for 3D structured samples), and the space-charge-suppression mode (repels the large amount of slow background electrons that may be photoemitted simultaneously). In the standard mode, photoemitted electrons are accelerated by a strong, uniform electric field (extractor field) toward the anode (Figure 2). Exploiting a general principle of microscopy, the reciprocal image or momentum-space image is formed in the Fourier plane of the objective lens, which is then magnified and projected onto a 2D detector. This concept provides some key capabilities and advantages for MM over traditional ARPES instrumentation as follows.

2.3.1. Capabilities and Advantages of MM

Imaging the Full 2D Momentum-Space: Due to the large extractor field between sample and objective, the photoemitted electrons follow a parabolic trajectory, as illustrated in the top left diagram in Figure 2. This results in the acceptance of a larger angle of photoelectrons into the aperture of the anode, compared to the case of no extractor field, as done in traditional ARPES measurements. For anode voltages on the order of several thousand volts, and sample-objective distances on the order of a few mm, the effective acceptance angle can be 2π , the solid angle describing a full hemisphere. Thus, all photoemitted electrons from the surface can be collected by the objective lens and imaged onto the detector in the reciprocal space, giving the technique its name—momentum microscopy. Unlike traditional ARPES instrumentation, one is not restricted to measuring just a limited region of the BZ in a given measurement. This has the potential to provide a more complete view of the electronic structure, without requiring a priori knowledge about the electronic structure.

Speed and Ease of Measurement: The ability of a cathode lens microscope to image the entire 2D reciprocal space in a single shot eliminates the need to tilt the sample or scan different axes to measure multiple high-symmetry axes of the BZ. This

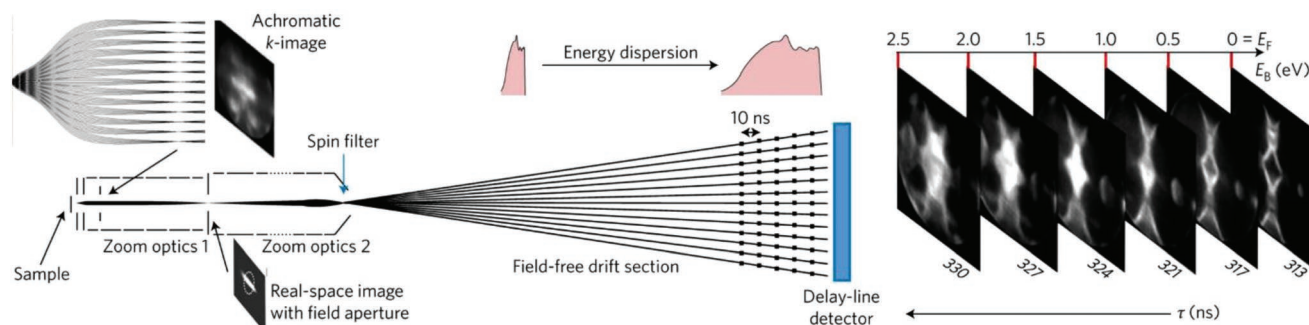


Figure 2. Schematic cross-section of a ToF-MM. The objective lens is biased with respect to the sample (far left of the scheme), collecting the photoemitted electrons from a wide angular aperture. Next in the MM, the back focal plane of the objective is imaged onto the detector using zoom optics 1 and 2. A real-space field aperture is introduced between the zoom optics. Then the electrons traverse a field-free drift section, before being detected in the Delay-line-detector (DLD). Their kinetic energy translates to time delays when arriving at the DLD, thus allowing to generate energy-resolved images of the impinging electrons as shown in the right edge of the scheme. Reproduced with permission.^[59] Copyright 2017, Nature Publishing Group.

results in a much faster measurement which is well suited for delicate samples.

Furthermore, in the reciprocal space image, the position on the detector linearly corresponds to k_{\parallel} and is independent of the kinetic energy (to within chromatic aberrations). Thus, unlike in ARPES using HA, the detector calibration and k_{\parallel} -resolution in MM do not change as a function of E_{kin} and k_{\parallel} .^[56,57]

Spatial Resolution: As a type of cathode lens microscopy, spatial resolution is inherent to MM. The objective lens not only forms a reciprocal image in the Fourier plane but also a real-space image in the image plane. Utilizing this intermediate real-space image, MMs can operate in three different powerful modes:

μ ARPES Mode: By placing an aperture (field aperture in Figure 2) in the image plane, one can selectively choose the region of the sample one wants to investigate. The aperture transmits only the photoelectrons from the selected sample area, without impacting the subsequent magnification and projection of the reciprocal image onto the detector. With aperture sizes on the micron scale, this allows one to perform μ ARPES measurements on the sample.

PEEM Mode: Alternately, instead of placing the field aperture in the image plane and projecting the reciprocal image on the detector, one can project the magnified real-space image itself on the detector. This allows the MM to operate as a photoemission electron microscope (PEEM), another powerful and versatile materials characterization technique that images photoelectrons with nanometer-scale spatial resolution. In fact, the technological basis for MM essentially is derived from PEEM, with microscope parameters optimized slightly toward the μ ARPES mode rather than PEEM. Thus, one can expect a similar level of versatility from an MM, as from a PEEM, albeit with potentially weaker spatial resolution, but likely higher energy resolution.

Dark Field PEEM Mode: Another powerful capability of PEEM that carries over to MM is dark-field imaging. In this mode, prior to acquiring the PEEM image above, one places an aperture in the Fourier plane to select a particular region of k -space. One can also choose a specific energy by spectral filtering. The image that is then formed on the detector derives only from that region in energy and k -space defined by the filter and aperture. In this mode, care needs to be taken regarding spherical

and chromatic aberrations in the imaging that increase when imaging photoelectrons away from the BZ center.

From the above discussion, it follows that MM, like PEEM, provides one of the key elements in studying 2D materials: the spatial resolution in a photoemission measurement. In the next section, we explain how MM provides a very attractive platform to include spin and time-resolution, thereby providing the ideal multidimensional photoemission spectrometer to study light-induced phenomena in 2D materials.

2.4. Multidimensional Photoemission Spectroscopy with MM

The earliest MM was demonstrated using an energy retarding filter, which succeeded in only mapping the Fermi surface of a sample.^[56] Subsequently, MM was demonstrated with double HA,^[58] which provided high energy- and momentum-resolution, along with spatial resolution. Here, we describe the operation of an MM utilizing a ToF spectrometer.^[59] Though double HA MMs have their own advantages of imaging the 2D momentum-space, the nature of the ToF spectrometer allows one to take full advantage of the MM's capability of imaging the full 3D energy-momentum (energy + 2D momentum) parameter-space as described below.

2.4.1. ToF-MM

In a ToF analyzer, to resolve the kinetic energy of the photoemitted electrons, they are allowed to drift through a suitably long, field-free section—the drift tube of the ToF detector—prior to arriving at the detector. Thereby, electrons of different kinetic energy arrive at different times at the 2D detector. By using such an appropriate delay-line-detector (DLD), one is able to discriminate between the arrival times of different electrons and thereby resolve their kinetic energy. The best reported resolution of such an apparatus is 9 meV^[60] (compared with 4.2 meV for single-HA MM), whereas with common drift tube lengths (≈ 1 m) and time resolutions of the DLD (≈ 150 ps), one can achieve energy resolutions on the order of a few tens of meV. An important point to note for DLDs is the dead time between two measurements. This leads to a maximum inte-

grable count rate, which is ≈ 8 Mcps in commercially available ToF-MMs.^[33]

Using a DLD to discriminate between the arrival time of electrons to resolve their kinetic energy, a ToF-MM necessarily needs a pulsed source that allows one to set the “start” time of the measurement. While a variety of pulsed sources can be used, this aspect makes ultrafast pulsed lasers very natural partners for ToF-MM. Their ability to bring in femtosecond time-resolution then makes time-resolved μ ARPES a natural possibility in MM, as discussed in Section 2.4.3.

2.4.2. SR-ToF-MM

Given the simultaneous 3D (2D k -space and energy) detection capabilities of ToF-MM, the recently developed multi-channel spin polarimeters become a natural choice for SR-ToF-MM. These polarimeters utilize the preservation of the 2D electron distribution in spin-polarized, low energy, electron diffraction, upon specular reflection from the surface of a high- Z crystal, such as Ir (001) and Ir (001) \times Au (1 \times 1). As shown in **Figure 3**, the spin analyzer crystal is placed to allow specular reflection into a second ToF branch which measures the spin-filtered image. The spin analyzer crystal is retractable, allowing rapid switching between the spin-integrated and spin-filtered image.^[33] This can be used to resolve both the spin “up” and “down” images. These schemes have recently enabled rapid acquisition of spin-filtered images on the order of a few minutes per image.^[33,61]

2.4.3. Time and Spin Resolved-ToF-MM

The scheme to incorporate femtosecond time-resolution into ToF-MM instruments remains essentially identical to conventional TR-ARPES measurements: a pump pulse excites the

sample, which is then probed by a time-delayed pulse that photoemits the electrons. While early TR-ARPES experiments with XUV photons utilized mJ-kHz class laser systems, TR-ToF-MM is well suited to take advantage of the newly appearing MHz class XUV generation systems. With their ability to eliminate space charge, and by operating close to the Mcps operational thresholds of ToF-MM, the MHz class lasers driving TR-ToF-MM measure electrons as efficiently as possible.

In the near future, one expects these time-resolved systems to combine with existing SR-ToF-MM (schematically shown in Figure 3), creating SR-TR-ToF-MM to provide a near-complete picture of the energy-momentum landscape of 2D materials and their heterostructures.

3. Exploring the Photo-Excited States with Momentum-Resolution: From Single- to Many-Particle Excitations

Having presented the evolution of the ARPES and ToF-MM instrumentation, we now turn to survey the discoveries these techniques have heralded in the excited state physics of 2D materials. In this section, we study the dominant photo-excited phenomena in TMDCs, including single-particle excitations, two-particle excitonic bound states, and collective phenomena. Traditionally, mapping the excited states of semiconductors and their dynamics has been realized using optical spectroscopy. However, since light carries a negligible momentum, it can only probe momentum-direct electronic transitions. Therefore, optical experiments can at best follow the dynamics of a sparse set of excited states. A wide variety of excitations in the BZ that are inaccessible to light remains literally in the dark. In contrast, time- and momentum-resolved characterization of the excited electronic band-structure can shed light on these excited states and their dynamics. Below, we discuss in more detail

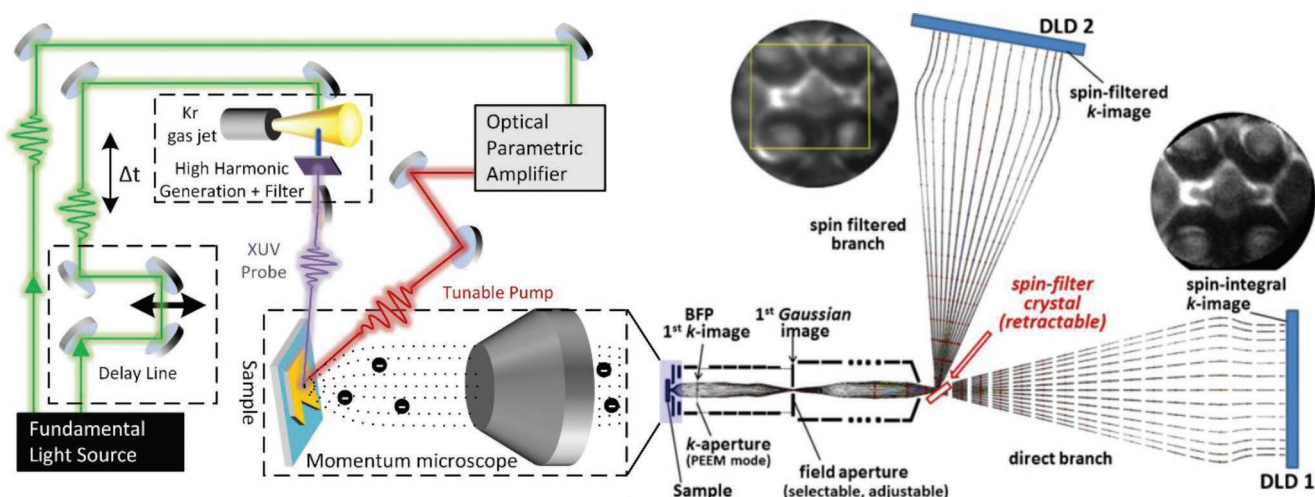


Figure 3. Schematic cross-section of an SR-TR-ToF MM. A spin filter (marked red) inserted at the entrance to the ToF detector deflects the photoemitted electrons of only one spin character onto a separate ToF detector. This gains an image of the sample band-structure with a specific spin component. Reproduced with permission.^[33] Copyright 2015, Elsevier B.V. The time-resolution can be implemented by the table-top apparatus depicted in the left part of the figure: A tunable optical pulse is generated from a pulsed laser source by optical parametric amplification. The delayed XUV probe (photoemission) pulse is generated based on the same source using high-harmonic generation.

the rich physics that one accesses with a momentum resolved probe.

3.1. Virtues of Momentum-Resolved Versus Optical Characterization of Excited States in 2D Materials

In 2D materials specifically, the enhanced Coulomb interactions lead to strong renormalization of the single-particle band-structure, to the dominance of excitons in photoexcitation, and to pronounced many-body correlation effects.

The rich physics associated with the renormalization of the conduction band (CB) states, such as changes in the effective mass due to dense excited state populations, is challenging to study with optics or other measurements like scanning tunneling spectroscopy.^[62–64] Instead, momentum resolution is needed to directly observe these many-body effects as they extend over the momentum-space. Likewise, momentum-resolving techniques are necessary for understanding and accessing the different regions of the BZ that photoexcited free carriers might scatter to, which is important for various optoelectronic applications.

The dominance of excitons in 2D materials creates previously unavailable opportunities—from their many-body interactions to their application and impact in photovoltaic cells, optical information storage, and other atomically thin optoelectronic devices. This promise merits the detailed study of these two-particle bosonic states. In particular, momentum-resolved investigations can reveal a wealth of information about the excitons that is inaccessible by their traditional optical spectroscopy and other techniques. To start with, light can only induce spin- and momentum-preserving electronic transitions, thus accessing only the so-called “bright” excitons with zero center-of-mass (COM) momentum, and zero net spin (such that the constituent CB and valence band (VB) states have co-aligned spins). In TMDCs, for example, optical measurements access efficiently the so-called K-K bright excitons, coupling spin-aligned electrons and holes that are both at the K (or both at the K′) valleys in the BZ. Excitons with significant COM momentum, with the electrons and holes in different valleys across the BZ (e.g., K-Q excitons corresponding to holes at the K valley and electrons in the Q valley, or at Γ -K excitons with holes at the BZ center and electrons at the K points), or with a finite net spin (e.g., spin-flip or anti-aligned-spin excitons), are dubbed “dark” as they are much harder to access optically.^[8] For example, the spin-flip excitons were optically evidenced either indirectly,^[7,65] or by using means like strong magnetic field,^[66,67] and unusual experimental geometries.^[68] From the perspective of dynamics, the ability of optical spectroscopy to probe only bright transitions leads to sparse mapping in momentum-space of various scattering processes of charge-carriers and excitons (e.g., two bright excitons that are perturbed at the beginning and the end of charge-transfer process,^[69] or some internal excitations of these excitons^[70]). **Figure 4a** illustrates the distributions of these various excitonic states across the BZ and highlights the distributions and dynamic processes that momentum-resolved spectroscopy can effectively investigate.

Momentum-resolved techniques can also access the internal structure of excitons—bright or dark, in unique ways. As

described in further detail in Section 3.3.1, at low intensities and low temperatures, the momentum resolved distribution of the photoemitted exciton-bound electron directly measures the distribution of the relative coordinate between the electron and hole in the momentum-space. The Fourier transform of this distribution to the real-space provides the spatial distributions of the electron and the hole relative to each other, that is, the exciton shape and size.

At higher temperatures, or for spatially confined excitons, momentum-resolved measurements of the exciton-bound electron and hole can also access the finite COM momentum of the exciton (see Section 3.3.1 for further details). With this access to the relative and COM coordinates of the excitonic wavefunctions, one can obtain a nearly holistic picture of this photoexcited particle.

Observing these relative and COM coordinate distributions of the excitons, and the exciton dynamics in the momentum-space, is valuable for many scientific and technological reasons. The use of bright excitons for communication and information applications requires knowing their formation process and their decay channels to momentum- or spin-dark excitons. As well, the full spatial structure, spin, and COM information on excitons can reveal their temperature, transport properties, and possible interactions with other excitons (e.g., by Auger processes^[71–73]) or with electrons in the lattice. Such knowledge is necessary to guide the generation of condensed exciton phases, and impact excitonic-induced phase transitions which may be useful for quantum applications of 2D materials.

Altogether, these overall virtues motivated the momentum-resolved characterization of photoexcited states in 2D materials (summarized in **Figure 4b** in comparison to the more traditional optical spectroscopy). We survey these efforts below, beginning with the early efforts that measured free charge-carriers.

3.2. Single Particle Excitations and Dynamics

Early TR-ARPES studies of 2D materials focused on the analysis of single-particle photoexcited charge-carriers. These experiments mainly explored the scattering dynamics of photoexcited electrons across the BZ in graphene^[74–76] or TMDCs in the bulk form.^[52,77–80] Subsequently, through the use of innovative sample growth techniques to make large-area 1L TMDC samples, a few pioneering TR-ARPES studies also began to be reported on them too.^[37,81,82]

A recurring theme in these studies was the rapid scattering (over a few tens of femtoseconds) of electrons away from the K valley, in which they were generated (**Figure 5a–c**). The electrons were either scattered to other valleys in the BZ, or to the (often metallic) substrate, by the charge-transfer process (**Figure 5b**). Other experiments have directly mapped the scattering processes of photoexcited electrons and holes between the K and K′ valleys in 1L^[82,83] and bulk^[84] TMDCs. There, circularly polarized light was used to initiate the K-valley polarization of electrons and holes. Then, the populations of the photoexcitations at the K or K′ valleys were probed by integrating the signal over the relevant momenta and energies around the CB or VB edges. These measurements show the correspondence between the valley index and circular

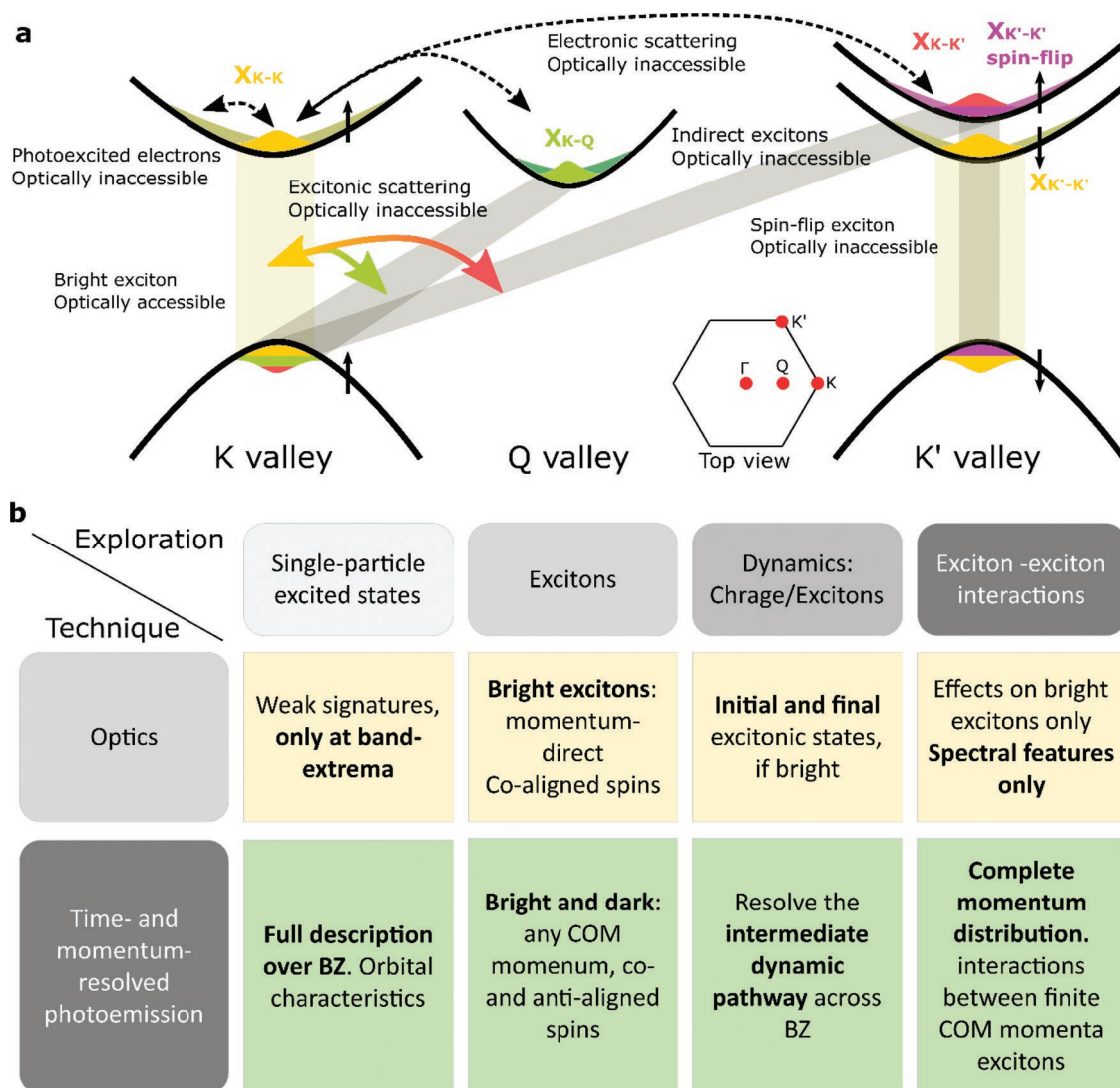


Figure 4. a) Schematic of various exciton states, conduction electron states, and their interactions and scattering pathways in monolayered TMDCs, demonstrating the optically accessible and inaccessible phenomena which could all be observed with TR-ARPES and TR-ToF-MM techniques. The bands spin near the K and K' points is indicated by short vertical arrows. While the spin-aligned K-K (and K'-K') excitons can be optically probed, the indirect K-Q and K-K' excitons, mixing holes and electrons of different valleys, and the spin-flip excitons, are inaccessible to light. Inset: Top view schematic of the hexagonal BZ of TMDCs with the K, K', Q, and BZ center (Γ) points marked. b) The virtues of momentum-resolved spectroscopy over optical spectroscopy in the study of monolayered semiconductors and the excitons they host.

polarization of the excitation (Figure 5d), as well as the valley lifetimes. Once more, electron scattering away from the K points was directly revealed as responsible for the rapid loss (<100 fs) of their valley polarization,^[84] as opposed to the holes that showed much slower depolarization.^[82,83] Further studies highlighted the role of momentum-scattering from the K and K' valleys across the BZ in the efficient process of charge-transfer to the substrate, specifically to 1L TMDCs^[78,85] or graphene^[86,87] that serve as the substrates in these experiments. These observations support the explanation of the interlayer charge-transfer robustness to layer misalignment,^[69,88] as follows. By phonon emission, the charge-carriers scatter from the K/K' valleys localized in one layer to other valleys in the BZ, where interlayer band hybridization is prominent and is weakly dependent on the layer alignment (Figure 6).

Additional phonon emission leads to further momentum and energy relaxation to the band edges at the K/K' points localized in the second layer, completing the charge-transfer process. Thus, the charge-transfer rate depends mostly on the momentum-scattering time scales.^[89]

Finally, TR-ARPES was also used to study many-body interactions between photoexcited free carriers and their manifestation in the band-structure of 2D materials. A few papers report the impact of Coulomb interactions leading to bandgap renormalization in 1L MoS₂^[90] and graphene/MoS₂ heterobilayers.^[91] Another effect is the change in the lattice structure mediated by electron-phonon interactions.^[92] Such interactions can also result in an electronic phase transition without modifying the lattice, such as insulator-metal transition^[93] or the loss of charge order in specific materials.^[94,95]

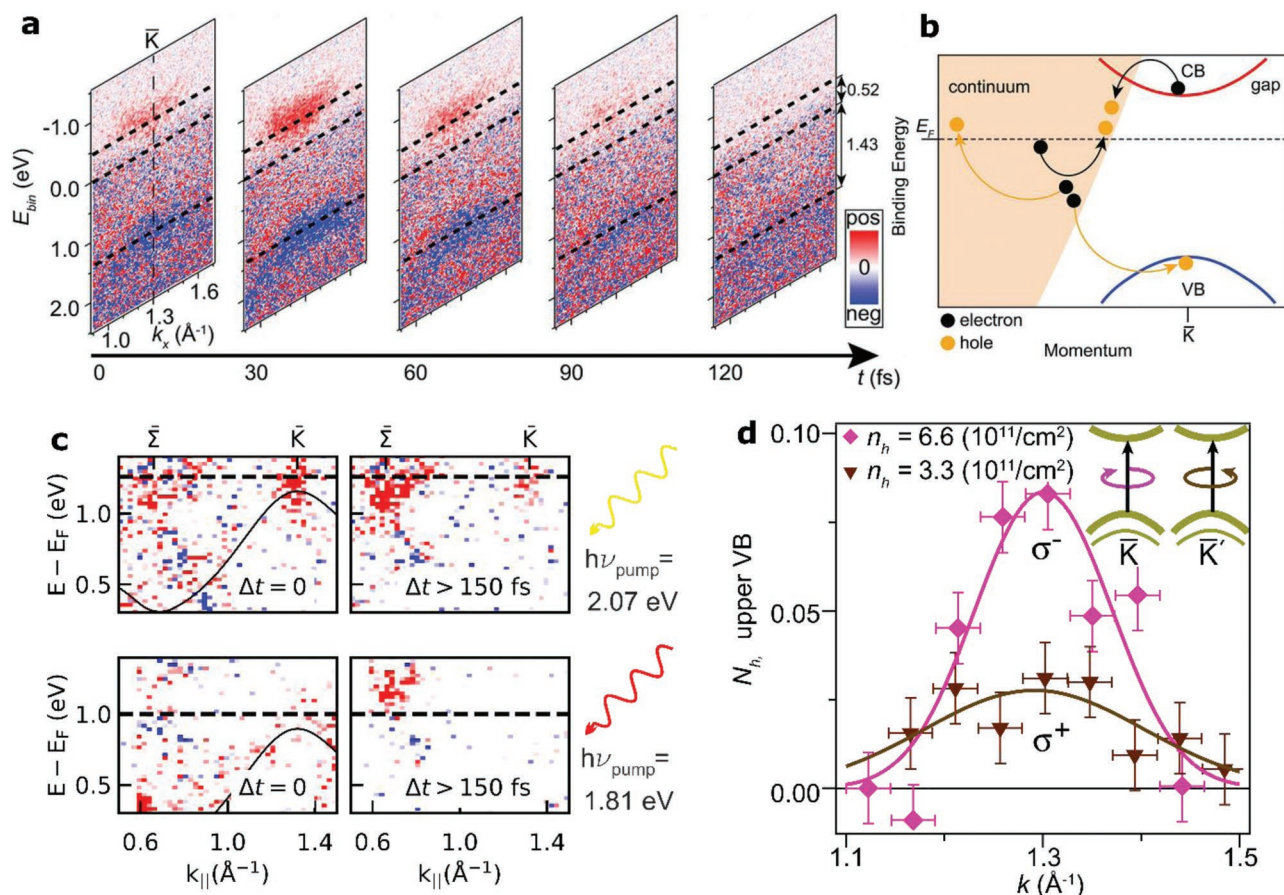


Figure 5. Charge-carrier scattering across the BZ. a) Differential TR-ARPES images of 1L-MoS₂ on Au(111) substrate, subtracting the unperturbed ARPES measurement from the data at increasing time delays, 2.0 eV excitation. Photoexcited unbound electrons (red clusters) and unbound holes (blue clusters) are generated at the K point and decay rapidly on a 50 fs timescale. b) Dynamic picture deduced from the observed transients. Charge-carriers scatter away from the K point, transfer to the gold substrate, and recombine. Panels (a) and (b) reproduced with permission.^[37] Copyright 2015, ACS Publications. c) Differential ARPES spectra of bulk MoS₂, at zero- and >150 fs time delays, when exciting at two different energies. In either case, the excitation results in photoexcited electron accumulation at the Q point (here referred to as Σ). Reproduced with permission.^[78] Copyright 2020, APS Publications. d) Valley control of the excited holes, indicated by an energy-integrated hole count around the K valley, when exciting with σ^- polarization (magenta diamonds) showing more holes than for σ^+ excitation (brown triangles). Reproduced with permission.^[82] Copyright 2017, APS Publications.

3.3. Momentum-Space Manifestation of Excitons

3.3.1. Predicted Signatures

The prevalence of excitons in the excited states of 2D materials has motivated their study in momentum-space with photoemission tools. This led to recent theoretical studies,^[96–100] seeking to understand the signatures of excitons in the momentum-resolved photoemission measurements and their interpretation in terms of the excitonic wavefunction structure, excitonic momentum distribution, etc.

We begin by noting that an excitonic state is made up of a superposition of Bloch electrons and holes in the CB and VB, respectively. For example, the wavefunction of a bright exciton at rest with zero COM momentum, $|\psi_X\rangle$, is given by

$$|\psi_X\rangle = \sum_k A_k c_{ck}^\dagger c_{vk} |0\rangle \quad (5)$$

where $c_{ck}^\dagger (c_{vk})$ represent the creation (annihilation) operators in the CB (VB) with wave-vector $\mathbf{k} = (k_x, k_y, 0)$, $|0\rangle$ is the ground state of the system with empty CB and filled VB, and the superposition coefficients, A_k , determine the momentum-space envelope function of the exciton. In the photoemission process, $|A_k|^2$ provides the probability of photoemitting an electron from the exciton with wave-vector \mathbf{k} . Thus, the momentum distribution of the photoemitted electron from the exciton corresponds to the distribution of A_k . The Fourier transform of A_k to the real-space, $A(\mathbf{r}_{e-h})$, then defines the spatial distributions of the electron and the hole relative to each other. For example, the spatial extent of $|A(\mathbf{r}_{e-h})|^2$ defines the size of the exciton.

For the photoemitted electron from the exciton, the conservation of energy and momentum in the photoemission process dictates an unusual energy-momentum dispersion. Consider an electron emitted from an exciton with zero COM momentum (energy $E_X^{Q=0}$), by a photon of energy $h\nu$, arriving in a free electron state with momentum k and kinetic energy (E_e). Such a

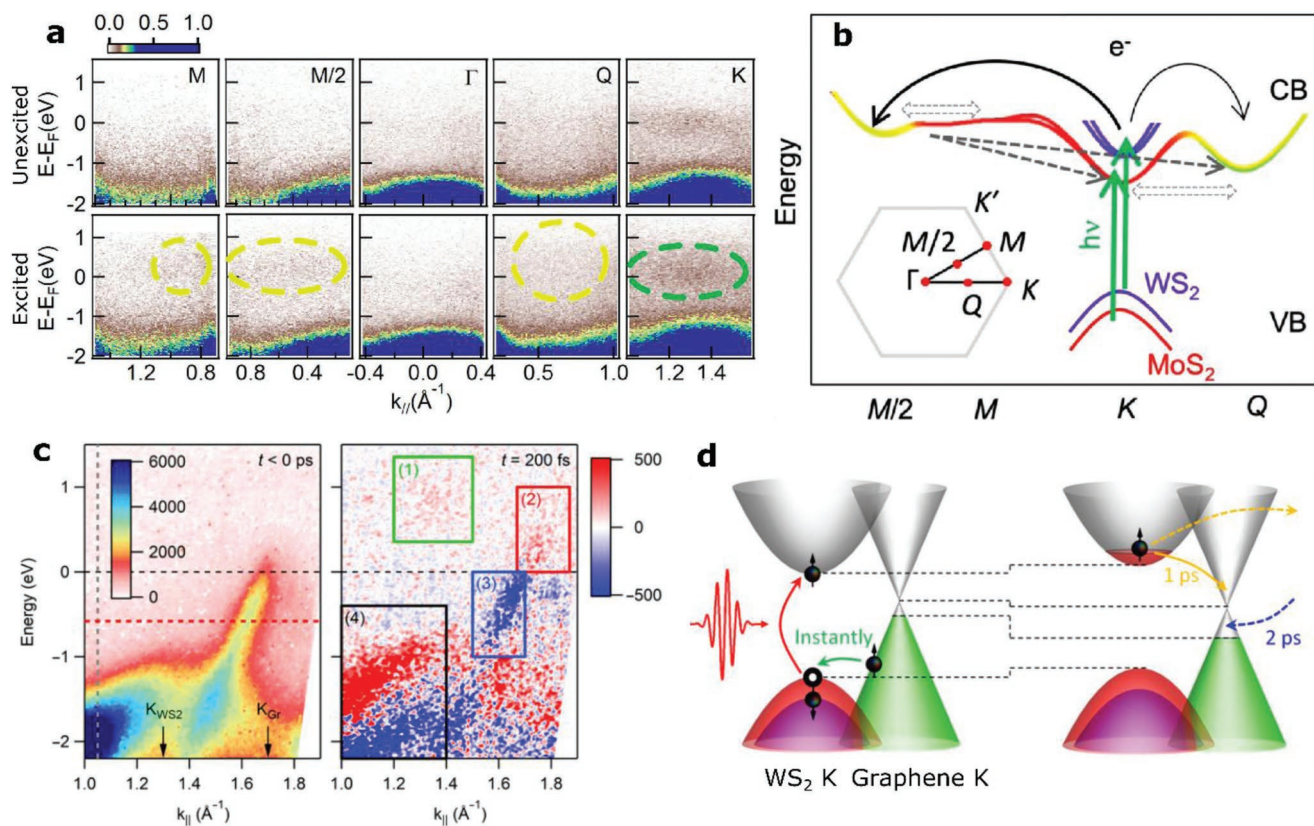


Figure 6. Charge-transfer pathways across the BZ. a) ARPES spectra taken without (top row) and with (bottom row) excitation around different points in the BZ of a MoS₂/WS₂ heterobilayer. Direct excitation at K is circled by a green dash. Transient populations at the Q, M, and M/2 points are circled with yellow dashes. b) The given interpretation of scattering from the K valley to the Q and M/2 valleys that allows hybridization-based transfer between the layers, thus being twist-angle robust. Both panels are reproduced with permission.^[85] Copyright 2020, APS Publications. c) Unexcited ARPES spectrum (left) and differential ARPES spectrum 200 fs after the excitation of a 1L-WS₂/graphene heterostructure. The differential spectrum shows excited electrons and holes in the graphene bands (marked (2) and (3) respectively), while WS₂ VB shows energy-shift signatures (marked (4)). There is a faint sign for photoexcited electrons in WS₂ (marked (1)). d) Interpretation schematics, showing the rapid hole transfer from WS₂ to graphene (left cartoon) whereas the electron transfer to graphene is slower. In either case, the charge-carriers scatter over the momentum-space to allow these transients. Panels (c) and (d) are reproduced with permission.^[86] Copyright 2020, AAAS.

process leaves behind a hole in the VB with momentum k and energy $\frac{\hbar^2 |k|^2}{2m_h}$. Here, the VB edge energy is set as a reference to 0. Via the conservation of energy, the photoemitted exciton-bound electrons will show the following dispersion^[96,98,99]

$$E_e(\mathbf{k}) = E_X^{Q=0} + \hbar\nu - \Phi - \frac{\hbar^2 |\mathbf{k}|^2}{2m_h} \quad (6)$$

with Φ being the workfunction of the material.

This dispersion peaks at $\mathbf{k} = 0$ wave-vector, at $E_X^{Q=0} + \hbar\nu - \Phi$, which is red-shifted by the binding energy with respect to the measured CB edge energy, $E_C + \hbar\nu - \Phi$. For $\mathbf{k} \neq 0$ the energy of the photoemitted electron is reduced by $-\frac{\hbar^2 |\mathbf{k}|^2}{2m_h}$, since more energy is retained by the recoiled hole. This dispersion, rather than mimicking the CB dispersion as expected for unbound electrons, looks like that of the VB, including the VB effective mass. This negative dispersion from the photoemitted electron is the hallmark of an exciton-bound electron.

The photoemission signatures for an exciton at finite temperature are more complex, and require taking into account the finite COM momentum— $\hbar\mathbf{Q}$, into the excitonic wavefunction

$$|\psi_{X,\mathbf{Q}}\rangle = \sum_{\mathbf{k}} A_{\mathbf{k}}^{\mathbf{Q}} c_{e,\mathbf{k}+\alpha\mathbf{Q}}^\dagger c_{v,\mathbf{k}-\beta\mathbf{Q}} |0\rangle \quad (7)$$

As in the case of a classical two-body composite particle, the COM momentum is divided between the electron and hole according to $\alpha = m_e/M$ and $\beta = m_h/M$, with $M = m_e + m_h$, m_h and m_e are effective masses of the VB and CB, respectively. Deriving the photoemission signatures of these excitons, a similar energy and momentum conservation analysis as above can be performed. However, this time one sums over excitons of different COM momenta, whose energies are given by the excitonic dispersion, $E_X^{Q=0} = E_X^{Q=0} + \frac{\hbar^2 \mathbf{Q}^2}{2M}$. Thus, the entire energy-momentum distribution of the photoemitted electron displays the above negatively curved dispersion, but mixed with the positively curved excitonic dispersion (See Figure 7b, comparing its

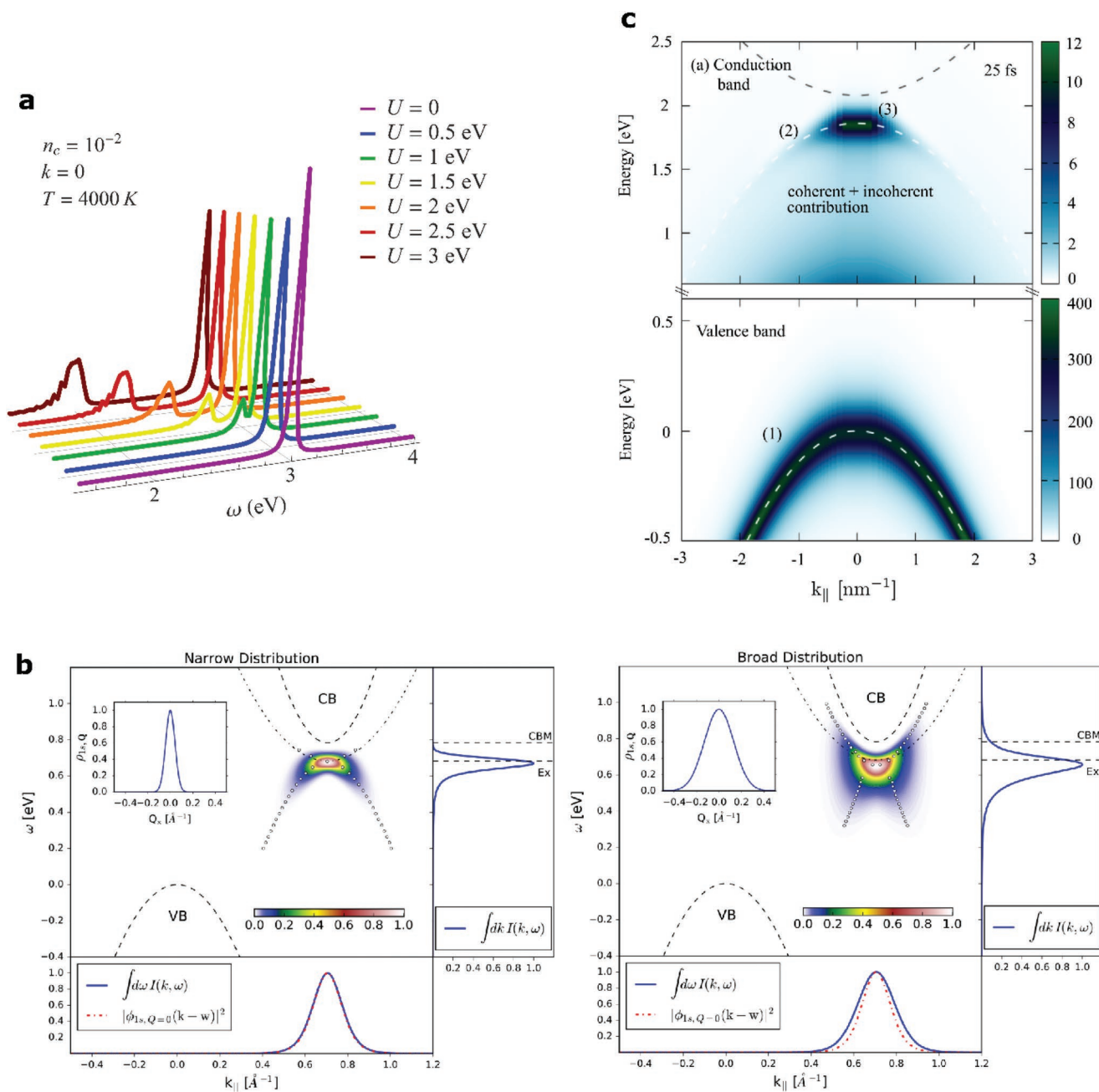


Figure 7. Predicted excitonic signatures in ARPES. a) The photoemission spectral function near the CB edge, calculated in ref. [96], showing the higher-energy band feature, and the lower-energy, exciton-bound electron feature. The latter appears at lower energies when the binding energy increases. Reproduced with permission.^[96] Copyright 2016, APS Publications. b) The anomalous dispersion of the exciton-bound electron signal (left), will be obscured by a thermal broadening (right). Reproduced with permission.^[98] Copyright 2018, APS Publications. c) The excitonic signature interferes with a replica of the VB. Thus, it is emphasized that to avoid such interferences, the examination of an excitonic signature must be at long time delays. Reproduced with permission.^[100] Copyright 2019, APS Publications.

left and right panels). This makes it more challenging to distinguish the hallmark exciton photoemission signature from that of the free CB electrons. Exciton–exciton interactions due to high photoexcitation densities, or rapid dynamical processes such as exciton–phonon scattering may also obscure the negative dispersion of the electron photoemitted from the exciton.

3.3.2. Experimental Requirements for the Detection and Identification of Excitonic Signatures

The above theoretical predictions provide a guide for the experimental conditions necessary to observe excitons and to distinguish them from free carriers. First, to observe the hallmark negative dispersion of the electron photoemitted from an

exciton, and to measure the intrinsic distribution of the relative electron-hole coordinate, one must probe a reasonably low density of excitons to avoid nonlinear exciton interactions. Additionally, low probe pulse intensities are important to avoid the effect of space-charge—the broadening in measured energy and momentum resolution caused by the Coulomb repulsion between the multiple electrons photoemitted by the same probe pulse (This effect is particularly serious in cathode-lens instruments like momentum-microscopes, as the extractor field pulls all the slow electrons into the microscope optics^[101]). One must also probe the excitonic population at a reasonable time delay after photoexcitation, so that a quasi-equilibrium state at a low enough temperature is achieved. Such a long time delay also helps to avoid the optically driven Floquet and Volkov replicas of the VB, which occur at zero time-delay^[96,97,100,102,103] (Figure 7c). Finally, the entire apparatus (measurement system and sample), must allow sufficient spectral resolution to reliably measure the anomalous negative dispersion, and to separate the photoemission signal of excitons from that of unbound electrons in the CB. With state-of-the-art detection setups, the bottleneck for achieving these resolutions is the inhomogeneity in the sample itself.

These requirements dictate experimental constraints on the sample size, its supporting substrate, the measurement spot size, and the laser repetition rate, as discussed below.

Sample Size: Typically, the larger a 1L 2D material flake is, the less uniform it is. Depending on its fabrication procedure, it may show polycrystalline domains, variable strain profiles, and inhomogeneous charge environments, together with chemical residues and impurities. Thus, to obtain as narrow a photoemission linewidth as possible, it is desired to employ small flakes, of high-quality crystals, typically no more than a few tens of microns across. Using such high-quality crystals also reduces the defect-related non-radiative recombination of excitons, prolonging their lifetime.

Measurement Spot Size: Measuring the photoemission signal from a small sample, or from just the small region of homogeneity in a sample, requires spatial resolution, often on the micron-scale, corresponding to typical sizes of the high quality exfoliated samples. This allows one to ensure that photoemitted electrons from background regions of the sample, containing inhomogeneities, bilayer regions, etc. do not contribute to the measurement.

Sample Substrate: In a photoemission measurement, the substrate of the sample acts as a charge reservoir, replenishing the electrons collected from the sample by the detection apparatus. As such, most samples interrogated to date have been supported directly by conductive substrates, like metals, highly doped silicon, or graphene.^[37,81,91] However, while efficiently replenishing the charge of the sample, the efficient charge-transfer also results in rapid excitonic decay times on the scale of tens of femtoseconds,^[69] making their observation challenging. Moreover, the metallic substrate screens the Coulomb interactions in the sample, reducing the excitonic binding energy, and quenching their optical signature.^[104] This obscures the benchmarking of the exciton photoemission with respect to its well-studied optical signatures (luminescence, absorption). Mitigating this problem can be done by introducing layers of insulating hBN between the semiconducting sample and the

conductive substrate. Furthermore, once hit by the XUV pulse, the photoexcited hBN provides a photoconductive path to the sample. More importantly, it allows a clear comparison of excitonic features without compromising their binding energies or lifetimes. Additionally, the flat interface with hBN offers improved homogeneity for the sample, as well as spacing it from the rough substrate and its potential charge puddles which can be a source of inhomogeneity.^[105]

Laser Repetition Rate: The immediate consequence of the desire to work with low pump and probe fluences is lower signal-to-noise levels. In order to recover or obtain a higher signal-to-noise ratio, one increases the repetition rate of the experiment beyond the common kHz domain. In a typical pump-probe based time-resolved experiment this rate is determined by the laser repetition rate.

The above constraints provide some insight into the inability of early TR-ARPES experiments on 2D semiconductors to observe clear excitonic signatures, given their lack of spatial resolution, corresponding use of large, inhomogeneous samples which needed to be grown on conductive substrates, and finally low signal-to-noise ratio due to kHz laser repetition rates. In contrast, multi-dimensional TR-ToF-MM is tailor-made to address these challenges. The platform inherently offers micron-scale spatial resolution, allowing the measurement of small homogeneous regions in high-quality samples. The spatial resolution and exfoliation technique also allow the easy incorporation of thin layers of insulating hBN between the sample and the conducting substrates. Finally, the MHz detection rates of the TR-ToF-MM became an ideal match for the recent developments in higher harmonic generation (HHG), which allowed MHz-rate generation of a reasonably high flux of XUV photons. Additionally, TR-ToF-MM offers a simultaneous and complete image of the full two-dimensional BZ of the sample, including a complete image of any excitonic features it stores. This provides more data for improved analysis of the observed features. Furthermore, it speeds up the measurement process (compared with mapping along high symmetry lines only as in TR-ARPES), avoiding drifts and damage to the sample. Together, this series of improvements led to the recent identification of the excitonic features in the momentum-space of TMDCs, heralding a chain of discoveries,^[106–110] as presented in the next section.

3.3.3. TR-ToF-MM Observations of Excitons

The first observation of excitons in exfoliated 1L WSe₂ supported by hBN substrate was achieved by Madéo et al., using a TR-ToF-MM apparatus.^[106] Photoexciting the sample exactly at its lowest-energy free-exciton resonance (so-called the A-exciton), well below the electronic bandgap, the authors observed excitonic features 1.73 eV above the VB edge around the K points (1.26 Å⁻¹ away from the BZ center). A short time delay later, they also observed the appearance of the momentum-indirect dark excitons in the Q-valley (0.75 Å⁻¹ away from the BZ center toward the K points, see Figure 8a–c), nearly degenerate with the K-valley signatures. These signals were associated with excitons based on the match to the exciton energy from photoluminescence and photoabsorption

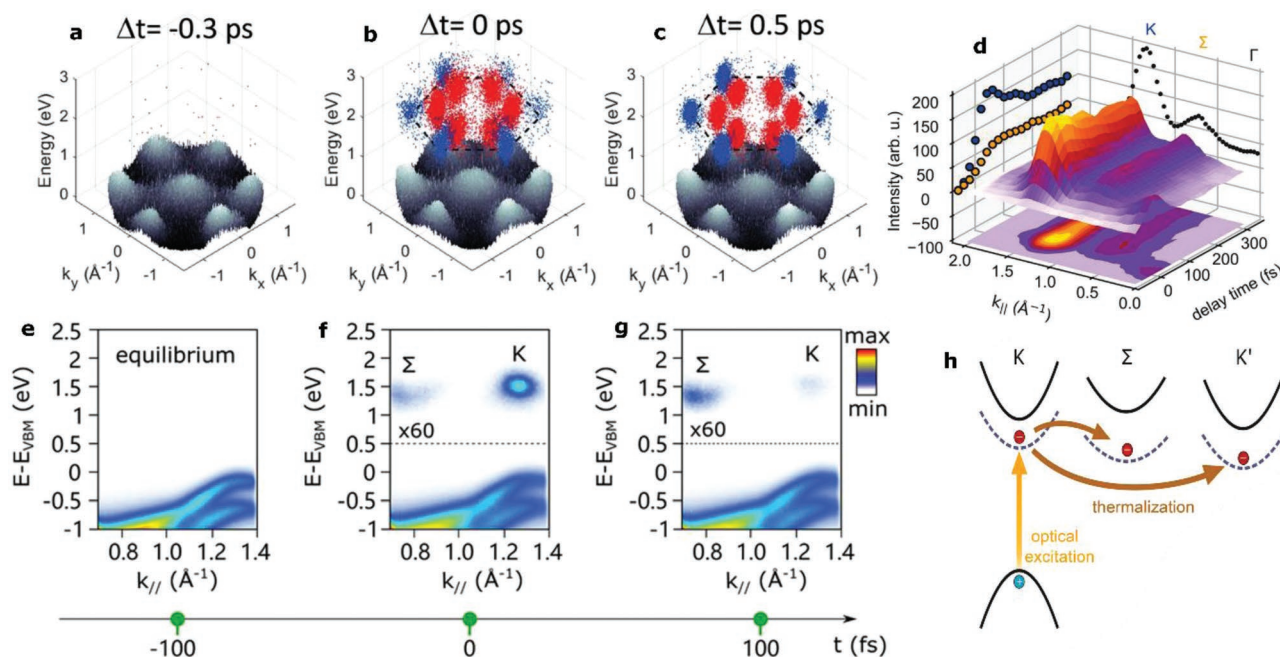


Figure 8. TR-ToF-MM identification of excitons in momentum-space and their dynamics. a–c) TR-ToF-MM spectra of the entire BZ of 1L- WSe_2 at different time delays with respect to the above-bandgap excitation. Within the experimental temporal resolution, excitons are formed at both the K (blue) and Q (red) valleys. Reproduced with permission.^[106] Copyright 2020, AAAS. d) High temporal resolution dynamics of excitons in the K and Q valleys of WS_2 showing the delay in the formation and accumulation of the Q-excitons with respect to the K-excitons, deducing a 16 fs scattering timescale at room temperature. Reproduced with permission.^[109] Copyright 2021, ACS Publications. e–g) Time-series of TR-ToF-MM spectra from a bulk WSe_2 , showing the excitation of excitons at K and their subsequent relaxation to the Q valley. Reproduced with permission.^[108] Copyright 2021, Wiley. h) Summary of the observed exciton dynamics: excitation at K-K, dominant scattering to K-Q, and additional scattering channel to a K-K' exciton. Reproduced with permission.^[109] Copyright 2021, ACS Publications.

spectroscopy (regarding the K-K exciton), along with the fact that sub-bandgap excitation at the A-exciton resonance, that cannot excite free charge-carriers, was used. Further corroboration was obtained through a photoemission excitation measurement—the photoemission analogue of a photoluminescence excitation (PLE) experiment. The resulting excitation spectrum produced exactly the exciton peaks and the onset of free carrier absorption that one obtains from an optical absorption measurement or PLE experiment.

The authors then followed the dynamics of formation, intervalley scattering, and subsequent decay for both the K-K and the K-Q excitons. With a temporal resolution of 180 fs, it was found that upon resonant excitation of the K-K exciton, the signal at the K point shows up seemingly instantaneously, while the K-Q exciton forms after ≈ 400 fs delay. In contrast, following excitation above the electronic bandgap, at 2.48 eV, both excitonic features appeared instantaneously, consistently with the sub-100 fs intervalley scattering timescales obtained for uncorrelated charge-carriers.^[37,81] The binding energies of both types of excitons were also estimated based on an ab-initio calculation of the CB edges at the K and Q points, in comparison to the observed excited signal energies. The binding energies were found to be 390 meV for the K-K exciton, and 480 meV for the K-Q exciton. This indicates that the observation of almost resonant photoemission features at the K and the Q points in the BZ is another fingerprint of their excitonic origins, different from the possible signal of CB electrons, which should have shown significantly different energies at the K and the Q points.

Two reports then followed up on this breakthrough of measuring exciton dynamics. Wallauer et al. studied the intervalley scattering dynamics of excitons in a 1L WS_2 with finer temporal resolution.^[109] The signatures of both the K-K and K-Q excitons were identified based on arguments similar to the previous report. Shorter excitation and photoemission pulses (≈ 50 fs resolution) were used to access the sub 100 fs dynamics of the observed excitons, shown in Figure 8d. Consistent with the measurements on 1L WSe_2 , a difference in the formation time-scales was found between resonant excitation of the K-K exciton and above-bandgap excitation. However, in the resonant excitation case, the formation of K-Q excitons was delayed by only 16 fs, much shorter time than in the 1L WSe_2 experiment, stemming from the temperature difference between the two experiments. The WSe_2 experiment was performed at 90 K, and the latter, WS_2 experiment, was done at room temperature, allowing for more efficient phonon-mediated intervalley scattering.^[8]

In parallel to the work by Wallauer et al., Dong, Puppini et al. used TR-ARPES and TR-ToF-MM to characterize the dynamics of excitons in WSe_2 in the bulk form.^[108] Such a measurement of a bulk sample benefits from increased signal strength, larger sample size, improved sample quality and no restrictions related to substrate. Yet, the electronic structure of the bulk differs from the 1L in critical ways. In particular, the electronic bandgap of the bulk material is indirect, it exhibits inversion symmetry that is not present in the 1L (thereby removing the spin/valley locking), and the Coulomb interactions in bulk

are reduced. Nevertheless, the bulk measurement can provide some important insights into the behavior of the 1L TMDCs. Similar to the 1L reports, the bulk measurements revealed the transient nature of the K-K excitons, that scatter rapidly, within ≈ 50 fs, in favor of the longer-lived K-Q excitons, as shown in Figure 8e–g. The signatures near the K points were identified as excitons by their appearance on resonance with a 1.55 eV excitation, whilst the CB signatures appeared at higher energies for above the bandgap, 3.1 eV, excitation. This difference was used to extract the excitonic binding energy. Figure 8h, taken from Ref. [109], illustrates the discussed scattering processes that were evident in this cluster of works.

Beyond the relaxation dynamics of excitons, the previously discussed theoretical studies elucidated a wealth of information that could be obtained from the momentum-resolved photoemission experiments on the two-body excitonic state. The high signal-to-noise of the TR-ToF-MM driven by MHz class table-top XUV generation capabilities now allowed a closer look at these predictions.^[107] Examination of the excitonic signatures at long time delays (after a few picoseconds) allowed one

to study excitonic distributions that have thermalized to a low enough lattice temperature, such that intrinsic excitonic effects were not dominated by thermal broadening effects. Additionally, the effects of exciton-exciton interactions were avoided by reducing the excitation fluence to an estimated exciton density of $\approx 10^{11}$ cm⁻², such that the estimated inter-exciton distance is much larger than their estimated radius. These conditions resulted in the first observation of the hallmark feature of excitons in a photoemission experiment: the anomalous dispersion of the exciton-bound electrons, shown in Figure 9a. Furthermore, by analyzing the excitonic envelope wavefunction in momentum-space (Figure 9b) and in real-space, an excitonic root-mean-square (RMS) radius was estimated by 1.4 nm (the real-space envelope function is imaged in Figure 9c). This value is consistent with the radius obtained by previous magneto-optical measurements^[111] with the differences explained by the differences in the dielectric screening between the samples.^[6,15] The subsequent measurements by Dong, Puppim et al. on the K-K exciton in bulk TMDCs obtained a Bohr radius of 1.74 nm, translating to an RMS radius of 2.13 nm,^[108] consistent with the

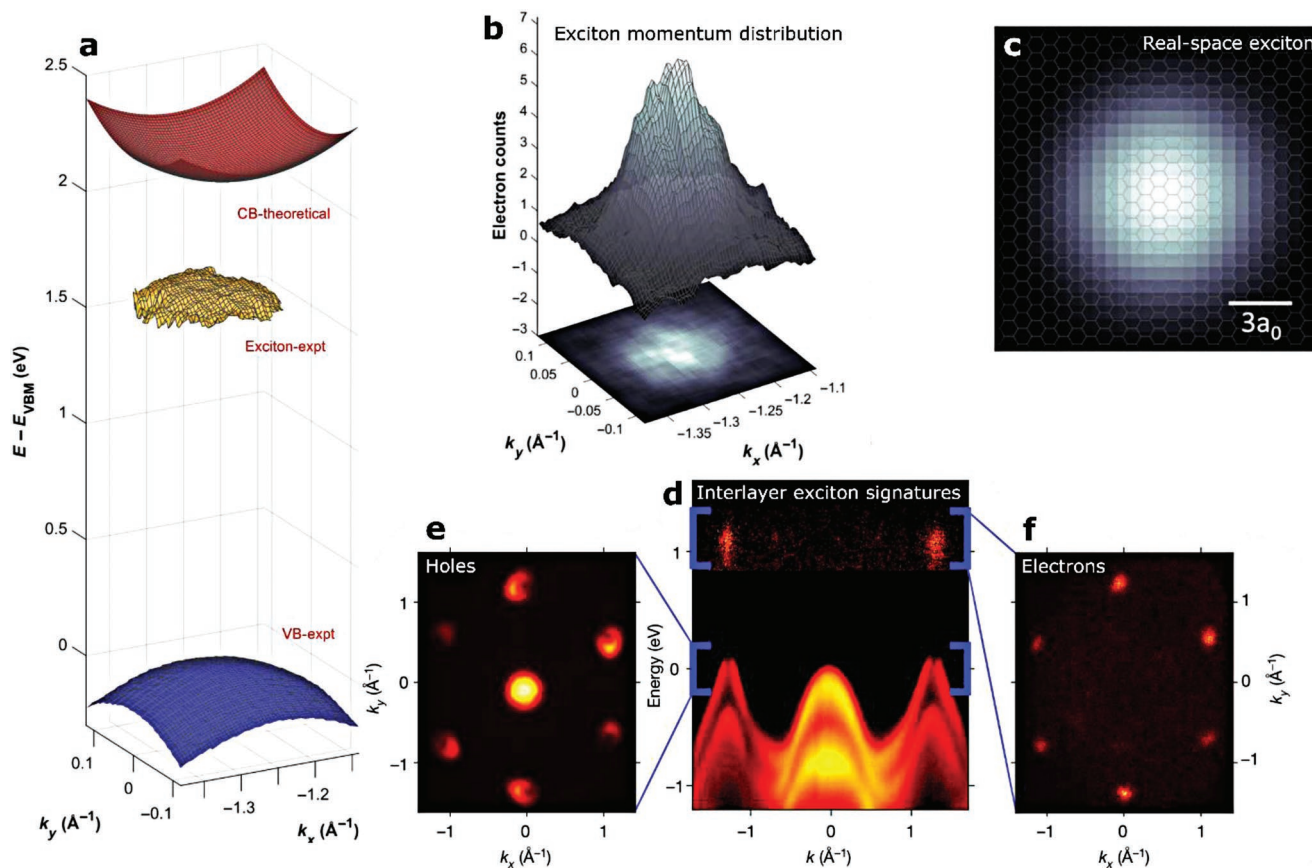


Figure 9. TR-ToF-MM studies of the exciton envelope function. a) A closer look at the fitted dispersion of the exciton-bound electron signatures around the K point of 1L WSe₂. The measured excitonic dispersion (yellow surface) mimics VB dispersion (blue surface) and is red-shifted by the exciton binding energy with respect to the calculated CB edge (red surface). b) The momentum distribution of the excitonic signature. Its width offers to deduce the real-space shape of the excitonic envelope function (modulus-squared). c) Real-space image of the excitonic envelope function. Panels (a)–(c) are reproduced with permission.^[107] Copyright 2021, AAAS. d) The energy-momentum cut of TR-ToF-MM measurement on a WSe₂/MoS₂ heterobilayer, revealing both the ILX-bound electrons and holes. e) Momentum-space image over the BZ of the VB edge energies, as marked by the blue brackets in (d). The holes are evident as ‘punctures’ in the band edge photoemission signal near the K points. f) Momentum-space image at the energy of the ILX, showing the clusters of the exciton-bound electrons near the K points. Panel (d)–(f) are reproduced with permission.^[110] Copyright 2022, Nature Publishing Group.

expectation of increased dielectric screening in bulk samples, which results in weaker excitonic binding.

Recently, TR-ToF-MM measurements enabled another breakthrough in excitonic studies,^[110] going beyond the existing theoretical predictions that describe only the exciton-bound electron photoemission.^[96–100] In these recent measurements, performed on the ILX of a heterobilayer of WSe₂ and MoS₂, the momentum distribution of both the exciton-bound electrons and the exciton-bound holes were resolved (See Figure 9d–f). The momentum resolved distribution of the holes was manifested by the absence of electrons at the top of the VB, as confirmed by an accompanying theoretical derivation. This measurement was enabled thanks to significant improvements in sample quality, and the ability to study the long-lived ILX.

The ability to measure the momentum distributions of both the constituent particles of the composite exciton accessed several key properties. Most importantly, it allowed the extraction of both the length scales that define the exciton: its relative electron-hole separation (i.e., its size), and the distribution of their common coordinate (i.e., localization of its COM). For the ILX, the measurement revealed the surprisingly tight COM confinement by the short-period moiré pattern of the heterobilayer. This suggested a resolution to an important conundrum in the technological application of ILXs such as arrays of single-photon emitters and correlated excitonic phases: It was believed that to confine large ILXs, large moiré unit-cells are needed. However, moiré lattices with large unit cells are inherently unstable and nonuniform, thus undermining the proposed applications that require uniform and stable arrays of confined moiré excitons. By showing that moiré lattices with small unit cells, that are more stable and uniform, can also tightly confine large ILXs, the work provided an important alternate path toward moiré exciton technologies.

In addition to size and COM localization, the simultaneous measurement of both the constituent particles of the exciton can provide a wealth of other information. A measurement of the momentum resolved distribution of the exciton-bound holes also directly provides the exciton density by comparing the VB photoemission signals before and after photoexcitation. One also directly obtains the valley configuration of the exciton-bound electron and hole in the BZ—an issue that remains under debate in many other TMDC heterobilayer systems.^[113,112,113] Finally, the measurement of the COM degree of freedom can reveal the temperature of the excitonic ensemble, as referred to in Section 3.4.

Similar to the work on intralayer excitons in 1L WSe₂, in the ILX work care was taken to ensure that thermal excitation and exciton–exciton interactions were negligible by performing the measurement in the low-density limit, at low temperatures, and at long time-delays. On increasing the photoexcitation intensity, an onset of exciton–exciton interactions was observed corresponding to a density of about one exciton per moiré unit cell, similar to the behavior of recently reported ILX complexes localized near defects.^[114,115] This points the way forward in exploring those many-exciton interactions, especially in the ILX context, due to their strong electric dipole fields and large sizes, that enhance the interaction with their surroundings.

Finally, Schmitt et al. studied the formation dynamics of ILXs in a twisted MoS₂/WSe₂ heterostructure, and showed the

modulation of the exciton-bound electron by the short-period moiré potential in that sample.^[116] This was enabled by the large twist angle in the examined sample (9.5°), translating to a large period of modulation in momentum-space ($\approx 0.2 \text{ \AA}^{-1}$), resolvable by the instrumentation. This report also followed the formation dynamics of such ILXs. Consistent with previous work surveyed here, it shows a charge-transfer process involving the Q (Σ) valleys in the BZ.

One property of the excitons that was missed in the above measurements is the phase profile of their wavefunction. The momentum- and real-space phase profiles are key for understanding the coupling of excitons from different localities, like neighboring moiré-trapped excitons, or hybridized excitons, that are coherent superpositions of intralayer excitons and ILXs. This information can be useful for manipulating those coupling mechanisms with light pulses. Furthermore, it is necessary for assessing the topological character of the excitonic transport. Recent work by Schüler et al.^[117] proposed a route for such characterization and demonstrated it on the Bloch (band) electronic states by modulating the polarization of the XUV probe pulse. Information on the orbital character and phase at each k-state is extracted from this measurement in combination with tight-binding models.

Another missing excitonic property in these measurements is the spin and valley character of the observed excitons. Due to the lack of spin-sensitivity in the above measurements, and the >100 meV linewidth broadening due to sample inhomogeneity, the signatures of the spin-aligned K-K and K-K' excitons and their spin-anti-aligned counterparts could not be distinguished from each other. To resolve these, future measurements will need to integrate spin resolution into the above capabilities (SR-TR-ToF-MM), use improved sample linewidths and higher spectral resolution (<10 meV), and utilize the dichroism in the photoemission matrix elements of different valleys (see for example refs. [117–119]). They will help address important aspects of spin and valley physics, such as spin-valley scattering, their transfer between the layers of a heterostructure, their utility as information carriers, and the role they may play in many-body exciton–exciton and exciton–free carrier interactions, which are discussed next.

3.4. Future Directions: Many-Body Effects Manifested in the Momentum-Space

Beyond the appearance of tightly bound two-body excitons, the enhanced Coulomb interactions in 2D materials also result in the formation of the next level of complexity in a few-particle bound excitonic states, such as the three-particle trions and four-particle bi-excitons.^[9,114,115,120,121] With increasing the exciton and free-carrier densities, one can generate increasingly complex multi-exciton states and exciton condensed phases,^[122,123] and corresponding multi-exciton phenomena such as exciton–exciton annihilation^[71,72] and Mott dissociation.^[124,125] These have been explored extensively, mostly from the viewpoint of optical experiments. These states and processes are important for fundamental studies, as well as for their varied applications, ranging from excitonic transistors,^[126] through photovoltaic cells,^[4] to quantum information processing.^[3] However, their

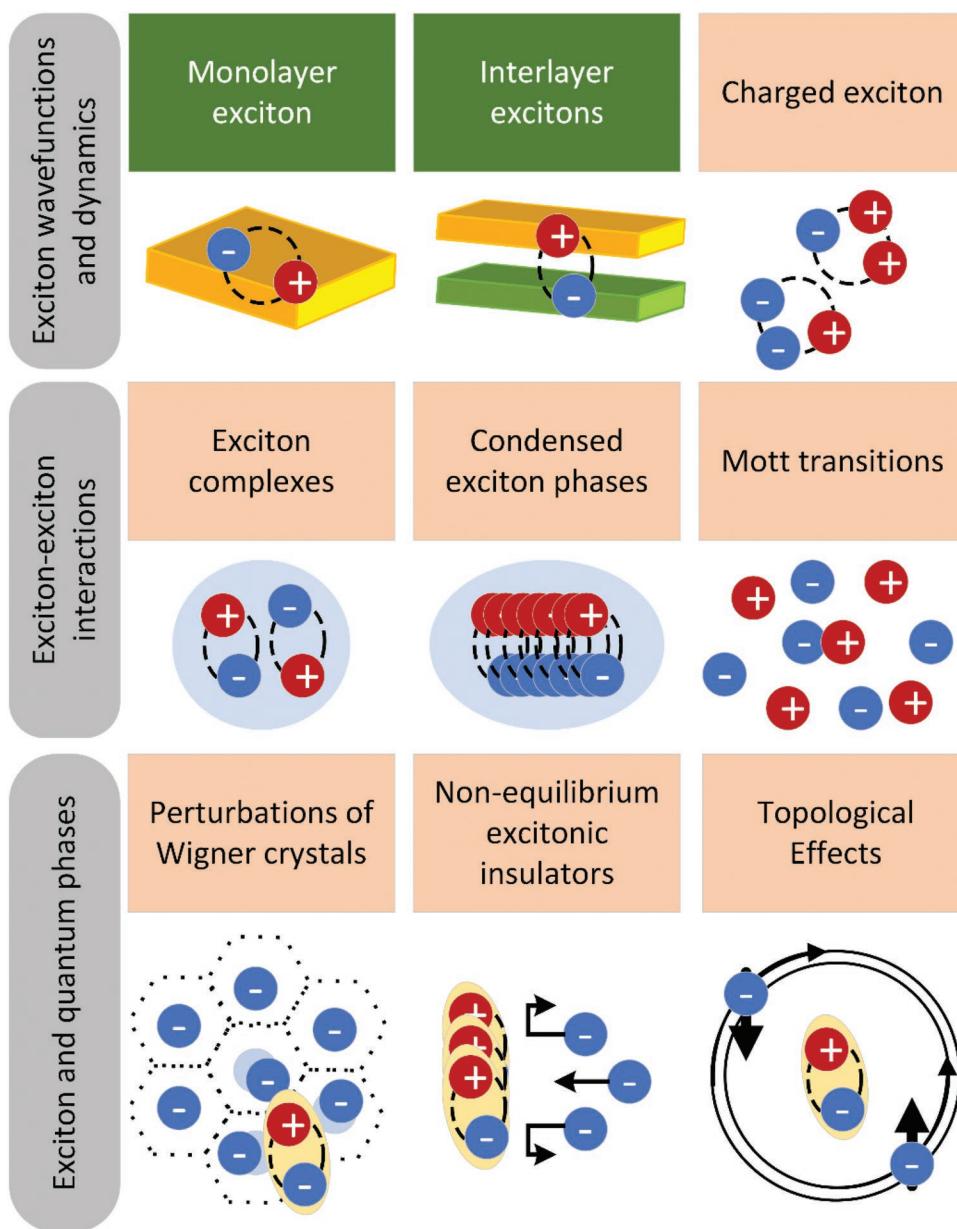


Figure 10. Prospective questions featuring excitons and their interactions. Top row: Excitonic wavefunctions for different excitonic species—single excitons, interlayer excitons, charged excitons. Middle row: Manifestations of many-exciton interactions—exciton complexes (e.g., bi-excitons), exciton liquids and condensed phases, and exciton dissociation processes. Bottom row: Excitons and quantum phases—excitonic perturbation of correlated electronic phases (Wigner Crystals), transient exciton insulator, and excitation-induced topological effects. Green rubrics indicate issues that have been recently addressed in experiments.

momentum degree of freedom has thus far remained largely inaccessible.

In going to momentum-resolved measurements of these phenomena with TR-ToF-MM, one can literally bring a new dimension to these important studies. **Figure 10** represents some of the potential directions to which TR-ToF-MM can contribute, starting from the completion of exciton species characterization and their dynamical interplay, followed by various manifestations of exciton-exciton interactions, and finishing with the impact of excitons and photoexcitations on the electronic band-structure

that may produce interesting quantum effects. As explained in Section 3.3.3, an important point to note about TR-ToF-MM measurements is their ability to quantitatively access the density and temperature of the photoexcited excitonic complexes—two parameters that are critical in understanding phase diagrams and many-body physics—both of which can only be crudely approximated in optical experiments.

In studying the momentum-space characterization of the few-particle exciton complexes like bi-excitons, trions,^[9,120,121] or their moiré equivalents,^[114,115,127] one can directly unveil the

valley configuration of the constituent electrons and holes, as well as deducing their spatial distribution relative to each other. Moreover, one can follow their formation, decay, and dissociation dynamics, and address questions regarding the interactions leading to their stable formation, as opposed to the processes of screening, dissociation, or Auger-type recombination.

In studying larger exciton ensembles that form condensed phases, like exciton liquids, and nonequilibrium exciton insulators, using MM, one can provide powerful complementary insight to the recent studies by electro-optical^[122] and capacitance measurements.^[123] TR-ToF-MM can directly characterize the excitonic states in such phases in both momentum- and in real-spaces, including valley/spin configurations of the constituent electrons and holes, spatial extent, and the impact of defects/domain boundaries on them. Additionally, the momentum-space perspective offers to clearly describe the band-structure of new materials with interaction-driven band gaps and nontrivial topologies, such as TMDC-based exciton insulators,^[128,129] superconductors,^[130] and generalized Wigner (and Mott) crystals reported in different stacks of graphene^[21,23] and in monolayers,^[131] homobilayers,^[25] and heterobilayers^[27,132–135] of TMDCs. In that context, TR-ToF-MM can assist the study of the excitonic impact on correlations in 2D materials. For example, given sufficient spectral resolution, TR-ToF-MM can follow the impact of excitonic populations on the band-structure in the presence of Wigner crystals. It can reveal the band-structure origins of recent excitation-based magnetism reported in a moiré system.^[136] Using the TR-PEEM mode of the TR-ToF-MM can reveal the spatio-temporal evolution of such effects, revealing the spatial extent of the correlations that lead to Wigner crystals formation, their properties, their kinetics, and their domain structure. Naturally, imaging the spin texture of these phases is essential for determining their nature, as has been suggested by various theoretical predictions.^[17,137]

Combining TR-ToF-MM with soft-X-ray energies in FEL facilities has the potential to reveal further information on excitation-driven property and phase tuning. For example, photoemission from the atomic core-levels can shed light on the Coulomb screening they experience from valence electrons as opposed to excitons,^[39] or identify charge-transfer between atomic sites in a lattice, to explain the emergence of excitation-induced magnetism.^[46] Adding the momentum-resolution, MM with soft-X-ray probe energies can describe the shape of the orbitals that make up the photoexcited states, as has been recently demonstrated for molecular compounds.^[40,138,139] It was shown, that even using XUV probe energies in combination with novel phase retrieval algorithms can already portray the orbitals of molecules.^[138,139] Higher energies, in the FEL range, can offer more complete coverage of the momentum-spread of such orbitals in 2D solids. With such a tool in hand, it will be possible to confirm the theoretical prediction about the character of the band states (e.g., whether they originate from p or d orbitals of some atom in the lattice). As well, upon excitation, it will be possible to correlate the band-structure modifications with population of electrons around different atomic sites, or with shape modifications of specific orbitals. These will give atomic-scale resolution in tracing the pathways of charge- and energy-transfer processes, or the formation of electronic order

in the lattice^[46] (producing effects like excitation induced magnetism, transient charge-density waves, etc.).

Finally, the temporal resolution of TR-ToF-MM measurements is advantageous for following the coherent dynamics of excitonic condensed phases and correlated phases in 2D materials. For example, coherent, spatio-temporal perturbations of exciton condensates may be explored by looking for their manifestations as satellite-replica (in momentum) of various features in the TR-ToF-MM data. The prospect of manipulating the band-structure, with or without generating excitations, is on its own a very attractive route for band-structure and topology engineering for quantum-computing applications. We dedicate Section 4 to fundamentally introduce the concepts of band topology and its coherent manipulation by light and photoexcited states, in the framework of Floquet band engineering.

4. Coherent Manipulation of the Band-Structure with Periodic Drives

4.1. Introduction

So far, we discussed transient quantum phenomena in 2D solids excited by short laser pulses, and how these phenomena can be observed using momentum imaging techniques. The external fields in this approach are used to drive the system into a transient excited state of the material and to probe it. Such pumping and probing techniques enable the mapping of the many-body spectrum of the static system and resolving the momentum, space, and spin structure of the excited states.

In this section, we outline an approach in which strong laser fields are employed to induce quasi-steady states that do not exist in the static spectrum of the system. This approach, often coined “Floquet band engineering,”^[140–143] gives rise to a fascinating possibility of designing and controlling electronic phases “on-demand.”^[144] It can be used for modification and fast switching of the fundamental characteristics of the material such as transport,^[145–148] magnetic,^[149–152] and optical properties.^[153–155] Furthermore, a periodic drive can induce non-equilibrium phenomena with no equilibrium counterpart, such as time crystals^[156–160] and anomalous phases defying edge-to-bulk correspondence.^[161–165]

Floquet phases are often associated with quasi-steady-state phenomena in the momentum-space. Therefore, imaging the momentum-space using TR-ToF-MM techniques can be invaluable for studying the underlying structure of these Floquet phases. Furthermore, the energy, momentum, and spatial resolutions of the TR-ToF-MM provide access to microscopic degrees of freedom and allow to study non-equilibrium phenomena, such as induced topological phases and thermalization and heating mechanisms.

Atomically thin vdW materials are particularly advantageous for Floquet engineering due to their 2D layout that allows for uniform illumination of the entire thickness of the material. Such a possibility is lacking in bulk 3D solids where external fields can only interact with states within a penetration depth that is often small. Another advantage of vdW materials is their versatility and variety of band-structures they feature, further extended by heterostacking.^[1,10] In such heterostructures, the modification of the

static band-structure of the constituent vdW materials combined with Floquet engineering gives rise to a wide variety of dynamical and static phases, known as the moiré-Floquet engineering.^[166]

4.1.1. Theoretical Model

We introduce a simple theoretical model, describing either a gapped or a gapless 2D system, which we use to demonstrate Floquet physics. While in the previous sections we focused mostly on TMDCs, in which the CB and VB are separated by a gap, in this section, we also consider semi-metallic (gapless) materials such as graphene. We include semi-metals in the discussion to demonstrate the unique topological phenomena that these materials exhibit under the application of the periodic drives. Furthermore, some of the recent solid-state Floquet experiments studied gapless systems such as graphene and surfaces of 3D topological insulators.^[102,103,167]

We consider a tight-binding model, minimally describing the low-energy spectrum of TMDCs or graphene, near the band edge in one of the valleys, located at $\mathbf{k} = \mathbf{K}$. Here, $\mathbf{k} = (k_x, k_y, 0)$ denotes the in-plane crystal momentum defined in the first BZ. Our model assumes a single degree of freedom for each crystal momentum, represented by the pseudospin states $|\uparrow\rangle$ and $|\downarrow\rangle$.^[31,168–170] The pseudospin states may denote orbital or sublattice indices, for example, in graphene,^[169] or a magnetic spin, such as for the surface states of Bi₂Se₃.^[171,172] The single-particle Hamiltonian for the crystal momentum \mathbf{k} is given by

$$H_0(\mathbf{k}) = \hbar v_F (\mathbf{k} - \mathbf{K}) \cdot \boldsymbol{\sigma} + m\sigma^z \quad (8)$$

where $\boldsymbol{\sigma} = (\sigma^x, \sigma^y, \sigma^z)$ is the Pauli vector acting in the pseudospin basis (e.g., $\sigma^x|\uparrow\rangle = |\downarrow\rangle$), and v_F and m are effective parameters respectively describing the group velocity and the mass gap of the electronic states. For $m \neq 0$, Equation (8) describes the CB and VB of a semiconductor with an energy gap of $2|m|$, whereas for $m = 0$, Equation (8) describes a semi-metal, exhibiting a gapless band-structure with a vanishing density of states at the band touching point, see **Figure 11c** for an illustration of the bandstructure. We note that the full band-structure of the vdW materials may host more than one valley, dictated by the crystal symmetries. Here, we assume an additional valley at $\mathbf{k} = \mathbf{K}'$, related to the valley at $\mathbf{k} = \mathbf{K}$ by time-reversal symmetry, see **Figure 11a**.

4.1.2. The Floquet Spectrum

To demonstrate the Floquet spectrum induced in the system by an optical drive, we first derive the Hamiltonian of the material in the presence of an external electromagnetic field. For concreteness, we assume illumination by right-handed circularly polarized electromagnetic field normally incident on the surface of the material, see illustration in **Figure 11b**. Such a field couples to electrons through the vector potential $\mathbf{A}(t) = A_0(\cos(\Omega t), \sin(\Omega t), 0)$, where $A_0 = \frac{E_0}{\Omega}$ with E_0 the amplitude of the incident electric field, $\Omega = 2\pi/T$ is the angular frequency and T is the period of oscillations in time. The Hamiltonian describing electrons interacting with the electromagnetic field, $H(\mathbf{k}, t)$,

can be then constructed by the minimal coupling, through a substitution $\mathbf{k} \rightarrow \mathbf{k} + \frac{e}{\hbar} \mathbf{A}(t)$ in $H_0(\mathbf{k})$, yielding $H(\mathbf{k}, t) = H_0(\mathbf{k} + \frac{e}{\hbar} \mathbf{A}(t))$. This Hamiltonian is explicitly time-dependent due to the time dependence of the vector potential. Furthermore, it has the same periodicity in time, T , as the laser field, satisfying $H(\mathbf{k}, t) = H(\mathbf{k}, t + T)$.

An explicit time periodicity in the Hamiltonian gives rise to non-equilibrium dynamics that cannot be generated by any static Hamiltonian. This dynamics is encoded in the Floquet–Bloch states,^[173] $|\Psi(\mathbf{k}, t)\rangle$, that are the solutions to the time-periodic Schrödinger equation

$$i\hbar \partial_t |\Psi(\mathbf{k}, t)\rangle = H(\mathbf{k}, t) |\Psi(\mathbf{k}, t)\rangle \quad (9)$$

Following the Floquet theorem,^[174] the Floquet–Bloch states can be expanded as a sum of harmonic terms oscillating in time with integer multiples of Ω ,

$$|\Psi(\mathbf{k}, t)\rangle = e^{\frac{i\varepsilon_{\mathbf{k}} t}{\hbar}} \sum_n |\Phi_n(\mathbf{k})\rangle e^{-in\Omega t} \quad (10)$$

Here $\varepsilon_{\mathbf{k}}$ and $|\Phi_n(\mathbf{k})\rangle$ are respectively the global phase factor and the partial wave of the n -th harmonic of the Floquet–Bloch wavefunction. Substitution of Equation (10) in Equation (9) results in a new eigenvalue problem that can be solved by a set of eigenstates $|\Psi_{\alpha}(\mathbf{k}, t)\rangle$, enumerated by the Floquet-band index, α , and eigenvalues $\varepsilon_{\mathbf{k}, \alpha}$ that are often denoted as the Floquet quasi energies. As follows from Equation (10), the Floquet quasi energy spectrum is periodic with a period of $\hbar\Omega$. **Figure 11e** demonstrates the Floquet quasi energy spectrum of $H(\mathbf{k}, t)$, for $m = 0$, along a cut in momentum $k_y = 0$, as a function of k_x . The black frame indicates a single replica of the Floquet spectrum in the energy range $\varepsilon \in \left(-\frac{\hbar\Omega}{2}, \frac{\hbar\Omega}{2}\right)$.

4.1.3. Detection of the Floquet Spectrum in Photoemission Experiments

The Floquet spectrum can be observed in photoemission experiments^[175–177] through the appearance of sidebands at the energies $\varepsilon_{\mathbf{k}, \alpha} + n\hbar\Omega$. The intensity of the sidebands is proportional to the overlap of the wavefunction of the probe and the partial waves $|\Phi_{n, \alpha}(\mathbf{k})\rangle$ defined in Equation (10). The amplitude of the partial waves rapidly decreases as a function of $|n|$, in the limit of a weak drive $e v_F |A_0| \ll \hbar\Omega$, such that only a few sidebands are usually visible in the photoemission signal. **Figure 11d** shows the calculated time-averaged density of states of $H(\mathbf{k}, t)$,^[178] demonstrating sidebands with intensity proportional to $\langle \Phi_{n, \alpha}(\mathbf{k}) | \Phi_{n, \alpha}(\mathbf{k}) \rangle$. The actual photoemission signal from these bands is additionally weighted by the band occupation.^[179,180]

The first observation of the Floquet spectrum of a driven solid was obtained using the TR-ARPES technique, on the surface of Bi₂Se₃ illuminated by midinfrared (MIR) light.^[103] The bulk of this material is a 3D topological insulator, hosting gapless surface states whose low energy physics can be described by Equation (8) with $m = 0$. The ARPES measurement of the surface before the pulse is shown in the leftmost panel of **Figure 11f**. During the pulse, new replicas of the original bands,

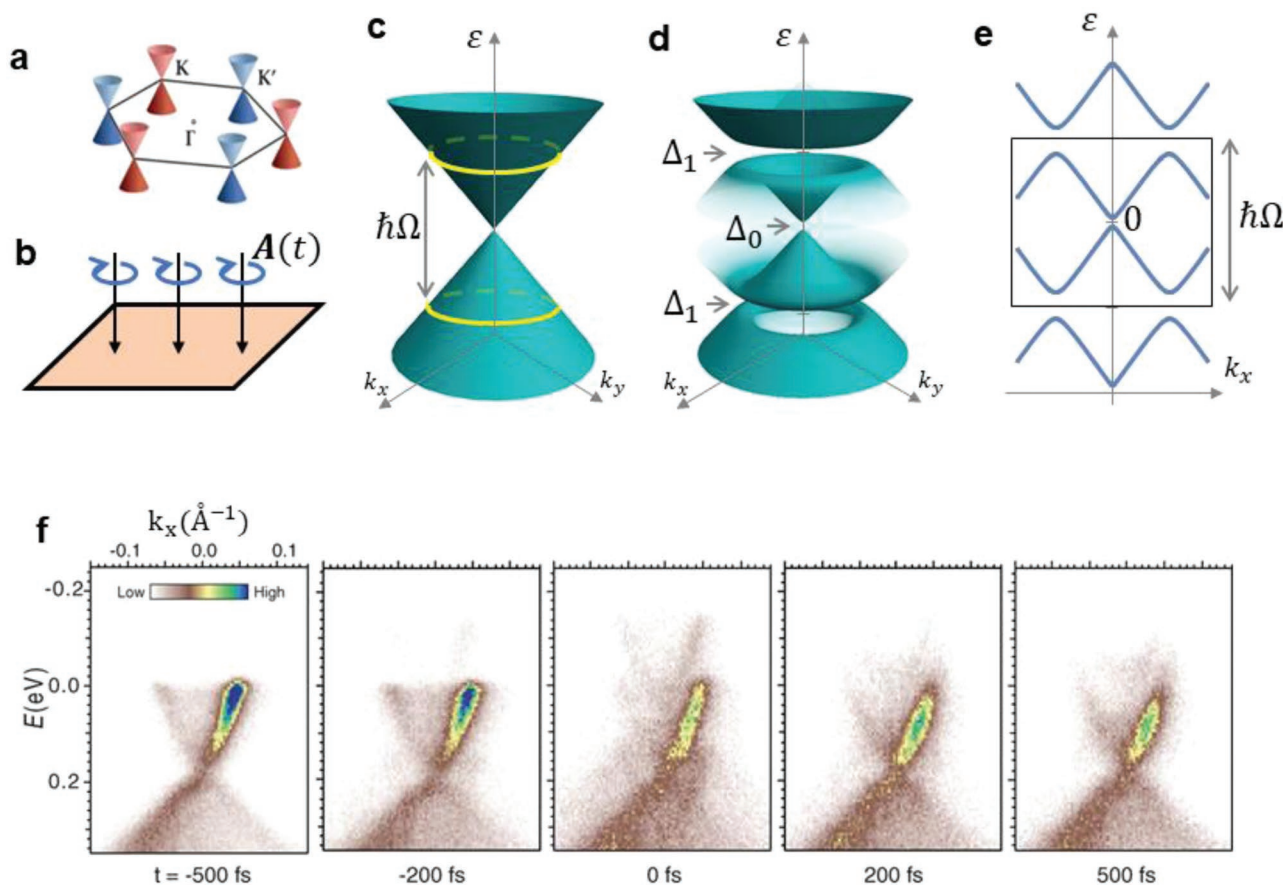


Figure 11. The Floquet spectrum in a semi-metal. a) An illustration of the BZ of a semi-metal like graphene. The BZ hosts Dirac cones (see Equation (8)) at K and K' points (Reproduced with permission.^[1] Copyright 2016, American Institute of Physics). b) Illustration of the setup, where a circularly polarized drive incident on the 2D material is used as an external drive, generating a Floquet spectrum. c) A single Dirac cone described by Equation (8) with $m = 0$, as a function of the in-plane momentum (k_x, k_y) . The yellow curves indicate the resonance rings describing states connected by a single photon of the drive with energy $\hbar\Omega$. d) The period averaged density of state of the Dirac cone driven with a circularly polarized light, exhibiting the Floquet bands separated by the resonant gaps at $\varepsilon = \pm\hbar\Omega/2$ of magnitude Δ_1 and an off-resonant gap at $\varepsilon = 0$, of magnitude Δ_0 . e) Floquet spectrum in (c) as a function of k_x , for $k_y = 0$. The Floquet spectrum has a periodic structure, with a period of $\hbar\Omega$. The black box indicates a single replica of the Floquet bands which repeats itself. f) TR-ARPES measurements of the spectrum of the surface of Bi_2Se_3 illuminated by a midinfrared (MIR) light, at different time-delays before and after the pulse (Reproduced with permission.^[103] Copyright 2013, AAAS). During the pulse (at 0 fs), one can observe the well pronounced Floquet replicas of the static band shifted by the multiples of the drive frequency.

shifted by the driving photon energy, $\hbar\Omega = 120$ meV, were observed (see the central panel of Figure 11f). For the electric field amplitude of 2.5×10^7 m^{-1} the measured Floquet spectrum exhibited dynamical gaps of $\Delta_0 = 53$ meV around $\varepsilon = 0$ and $\Delta_1 = 62$ meV around $\varepsilon = \pm\hbar\Omega/2$ (see Figure 11d and discussion below).

Besides the Floquet spectrum, a closely related effect, known as the Volkov states, has similar spectroscopic signatures in photoemission measurements. The Volkov states are eigenstates of free-electrons in a vacuum interacting with the electromagnetic field, hence exhibiting replicas of the free-electron spectrum, shifted by the same energy offsets as the Floquet bands. These states are distinct from the Floquet bands as they arise from the free states and thus do not depend on the symmetries of the crystal. In general, both the Floquet and Volkov states can appear in a spectroscopic experiment. Therefore, it

is important to be able to discriminate between them. The discrimination between the Floquet and Volkov states has been demonstrated by Mahmood et al.,^[102] by measuring the dependence of the measured spectrum on the polarization of the drive.

4.2. Floquet Engineering: Driving Topology with Periodic Fields

Having established the Floquet–Bloch states and the Floquet spectrum, we are in a position to discuss the properties and implications of the induced spectrum. One of the key motivations in the field of Floquet engineering is the perspective of inducing topological phenomena in trivial-band materials.^[146,147,181–186] This is an exciting perspective that enables controlling and fast switching of topological properties of the material by illuminating it with laser light.

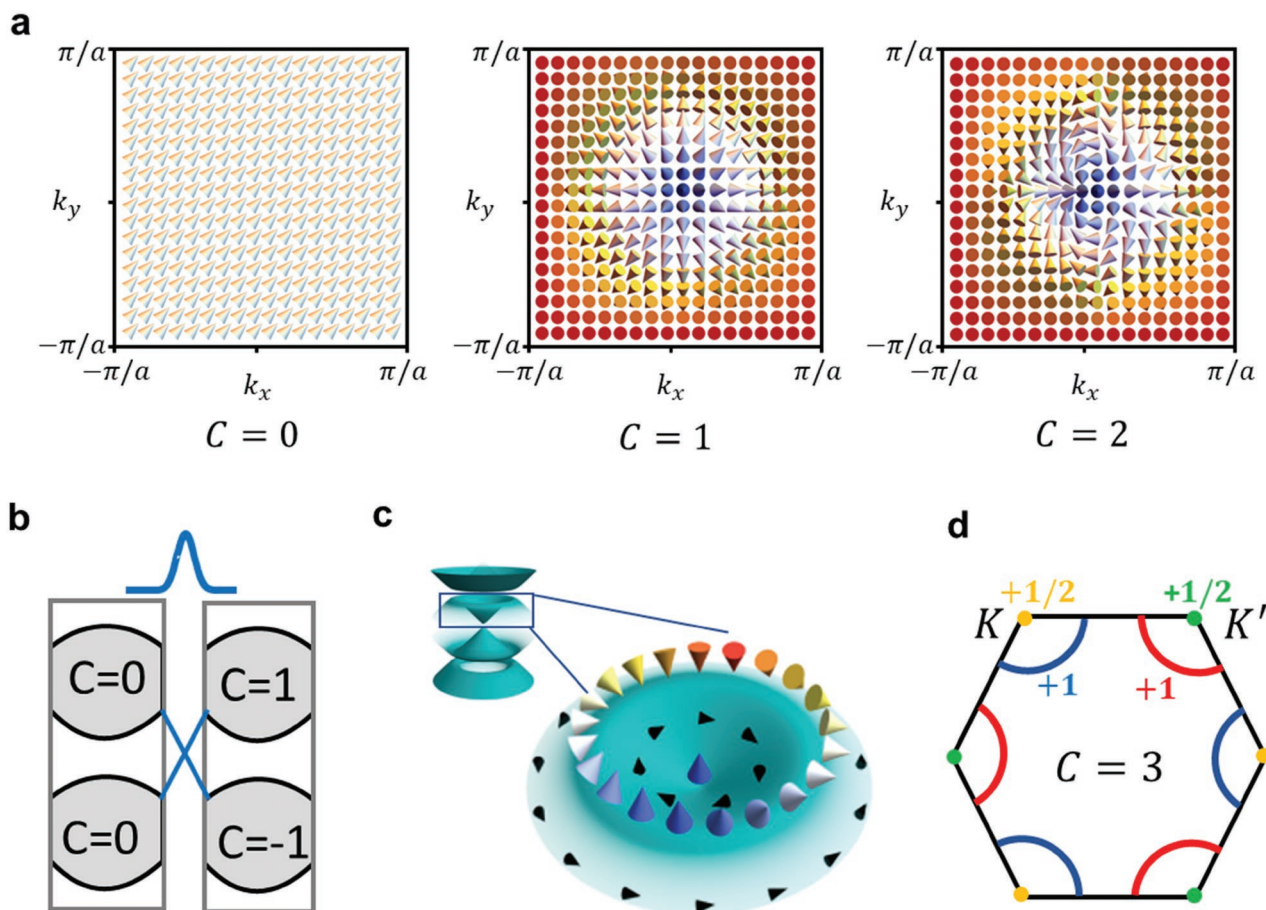


Figure 12. Pseudospin patterns in the topological and trivial bands. a) Illustrations of pseudospin patterns in the quadratic BZ corresponding to a trivial phase with a zero Chern number (left) and topological phases with Chern numbers 1 (center) and 2 (right). b) An interface of a system with topological bands with Chern numbers 1 and -1 and trivial bands with all Chern numbers zeros. To smoothly connect the Chern numbers on the left and right, the gap must host subgap states with a wavefunction localized at the interface. c) The pseudospin texture induced by the periodic drive (for a fixed gauge) near the K-point in the Floquet band indicated by the box on the left. Black arrows indicate the pseudospin texture of the states far from the resonance ring and the $k = 0$ point. The pseudospins indicated by black arrows in the inner ring correspond to CB, whereas the pseudospins indicated by black arrows in the outer ring correspond to the replica of the VB (RVB). Colored arrows indicate the pseudospins at the resonance ring, resulting from the hybridization of the pseudospins in CB and RVB. The blue arrow in the center indicates the pseudospin direction induced by the off-resonant effect of the drive. d) The BZ of graphene. Blue and red curves indicate the resonance rings around the K and K' valleys, each contributing 1 to the Chern number. Green and orange points indicate the momenta where the off-resonant transitions are dominant, each dot contributes $1/2$ to the Chern number. The overall contribution to the Chern number of the band sums up to $C = 3$.

4.2.1. Band Topology of the Floquet Systems

The topology of the Floquet bands^[146,147,187] can be classified by integer invariants called Chern numbers, which we define below. For concreteness, we focus on the model described by Equation (8) and Section 4.1.1 with Floquet bands $\epsilon_{k,\alpha}$ and Floquet–Bloch states $|\Psi_\alpha(\mathbf{k},t)\rangle$, denoted by the index α . We assume that the Floquet bands are separated by an energy gap, whose existence is crucial for defining the Chern numbers. It is convenient to define the Chern numbers through unit vectors pointing in the direction of the pseudospin of the Floquet–Bloch state of momentum \mathbf{k} and Floquet band α , $\mathbf{n}_\alpha(\mathbf{k},t) = \langle \Psi_\alpha(\mathbf{k},t) | \boldsymbol{\sigma} | \Psi_\alpha(\mathbf{k},t) \rangle$. The unit vectors $\mathbf{n}_\alpha(\mathbf{k},t)$ form a pattern as a function of \mathbf{k} in the BZ and a given band index α , which can correspond to either trivial or non-trivial topology. Different types of patterns are classified by

the Chern numbers, with a zero Chern number corresponding to a trivial pattern and non-zero integers otherwise. **Figure 12a** shows examples of pseudospin patterns on a square BZ for three distinct topological phases with Chern numbers zero, one, and two. A precise mathematical definition of the Chern number can be obtained in terms of the Berry curvature, measuring the solid angle covered by \mathbf{n}_α per unit of area in the momentum-space,

$$B_\alpha(\mathbf{k},t) = \mathbf{n}_\alpha(\mathbf{k},t) \cdot [\partial_{k_x} \mathbf{n}_\alpha(\mathbf{k},t) \times \partial_{k_y} \mathbf{n}_\alpha(\mathbf{k},t)] \quad (11)$$

The Chern number of the Floquet band α , is defined as $C_\alpha = \frac{1}{4\pi} \int_{\text{BZ}} d^2k B_\alpha(\mathbf{k},t)$.

By this definition, the integral of $B_\alpha(\mathbf{k},t)$ over the BZ must be an integer multiplied by 4π for any analytic $\mathbf{n}_\alpha(\mathbf{k},t)$.

Classification of the band topology by integer invariants suggests the robustness of these phases to small local perturbations. To change the topological invariant of the band, the perturbation must be sufficient to close the bandgap (given the perturbation does not break the symmetries protecting the topological phase). An important consequence of this fact is the emergence of subgap states at the interface between a system with nontrivial Floquet bands and a trivial system. The only way to connect the nonzero integer Chern number on the topological side and the zero Chern number on the trivial side is by the closing the bandgap at the interface between them. The gap closing is associated with the appearance of subgap states localized at the interface with exponentially decaying tails, see Figure 12b. These interface states are characterized by well-defined chirality,^[188] and give rise to unique transport properties such as the quantized anomalous Hall effect,^[189] quantized edge conductance, and the lack of backscattering.^[190]

Having established the notion of topology in the Floquet bands, based on the pseudospin patterns in the BZ, we can discuss how non-trivial pseudospin patterns can be induced by the periodic electromagnetic drive. We consider two main mechanisms for regulating the pseudospin textures in driven materials: the resonant and off-resonant topological transitions. These two types of transitions occur at different locations in the BZ: The resonant transitions occur in semi-metals and insulators near the curve in the momentum-space where the resonance conditions are satisfied. The off-resonant transitions occur only in semi-metals, at the gap closing point. To capture both resonant and off-resonant effects in the same model, we will focus on a driven semi-metal, described by Equation (8) with $m = 0$. Considering a semi-metal is also motivated by the recent experiment by McIver et al.,^[167] which demonstrated signatures of the drive-induced topology in MIR-illuminated graphene.

4.2.2. Resonant Floquet Topological Transitions

We begin by discussing resonant topological transitions, that occur when the drive is in resonance with transitions from CB to VB. Such resonances exist when the energy of the driving photon is smaller than the full bandwidth of the undriven system and larger than its bandgap (The second condition is always satisfied in semi-metals). For a resonant drive, the CB and the replica of the VB (RVB), shifted by $\hbar\Omega$, intersect, forming a curve in the BZ, which we denote as the resonance curve. For the band-structure in Equation (8), the resonance curve is a ring of radius k_R , encircling $\mathbf{k} = \mathbf{K}$ (see the yellow curve in Figure 11c), which we parametrize by an angle $\theta \in [0, 2\pi)$, such that the resonance curve is given by the momentum coordinates $\mathbf{k}_R(\theta) = (k_R \cos \theta, k_R \sin \theta) + \mathbf{K}$.

In addition to creating the replica band, the drive also opens a gap at the intersection of the CB and RVB, which is denoted as the Floquet gap (indicated by Δ_1 in Figure 11c). The eigenstates near the Floquet gap are superpositions of the states in the CB and the RVB. Importantly, the superposition states have a different pseudospin texture than the pseudospin textures of the CB or RVB alone, see Figure 12c. Furthermore, the pseudospin texture of the hybridized bands may have a different topology,

meaning that the drive induced a topological transition. To find the topological invariant of the induced pseudospin texture, we examine the effective Hamiltonian describing the CB-RVB intersection at the resonance curve, $\mathbf{k} = \mathbf{k}_R$, given in the basis of the non-hybridized CB and RVB wavefunctions, $|\psi_{CB}(\mathbf{k})\rangle$ and $|\psi_{RVB}(\mathbf{k})\rangle$,

$$H_R(\mathbf{k}_R(\theta)) = \begin{pmatrix} 0 & V_R(\theta) \\ V_R^\dagger(\theta) & 0 \end{pmatrix} \quad (12)$$

Here we shifted the energy to zero at the level crossing point for clarity. It can be shown that the off-diagonal term is given by the first frequency harmonic of the full Hamiltonian,

$V_R(\theta) = \langle \psi_{CB}(\mathbf{k}_R) | H^{(1)}(\mathbf{k}_R) | \psi_{RVB}(\mathbf{k}_R) \rangle$, where $H^{(m)}(\mathbf{k}) = \frac{1}{T} \int_0^T dt e^{im\omega t} H(\mathbf{k}, t)$ and $|\psi_{RVB}(\mathbf{k}_R)\rangle$ is the wavefunction of the VB. Notice that $V_R(\theta)$ is linearly proportional to the electric field of the driving beam, E_0 , as follows from the definition of $H(\mathbf{k}, t)$ in Section 4.1.2.

A diagonalization of $H_R(\mathbf{k}_R)$, yields the Floquet gap $\Delta_1 = |V_R(\theta)|$ and the Floquet–Bloch states at $\mathbf{k} = \mathbf{k}_R$. The term $V_R(\theta) = |V_R| e^{i\varphi(\theta)}$, determines the amplitudes and the relative phase of the CB and RVB wavefunctions constituting the Floquet–Bloch states. In particular, the complex phase, $\varphi(\theta)$, determines the orientation of the pseudospin $\mathbf{n}_\alpha(\mathbf{k}_R)$ of the Floquet–Bloch states as a function of θ along the resonance curve. It can be shown that for the model described in Section 4.1.2, $\varphi(\theta) \propto \theta$, corresponding to a single winding of the pseudospin along the resonance curve. As a result, the contribution to the Chern number from the pseudospin winding around the valley \mathbf{K} is 1. We note that a similar effect occurs in the valley \mathbf{K}' , resulting in a total contribution of 2 to the Chern number for a circularly polarized drive.

To resolve the topological structure in the experiments, the gap Δ_1 should be larger than the inverse characteristic lifetime of the Floquet–Bloch states in the material. This lower bound on the Floquet gap sets the lower bound on the intensity that can be used in the experiments, due to the dependence of Δ_1 in the driving field. In this context, the limitations on the visibility of the Floquet–Bloch states in the presence of scattering were studied in WSe₂ and graphene.^[191]

4.2.3. Off-Resonant Floquet Topological Transitions

Next, we consider the off-resonant topological transitions, occurring in semi-metals driven by circularly polarized light. The primary effect of the off-resonant phenomenon is the opening of a gap Δ_0 at the momentum where the undriven material has a gap-closing point (at $\mathbf{k} = \mathbf{K}$ in the model in Equation (8)), see Figure 11d. The gap opening is crucial for the topological classification of the CB and VB because the Chern number can be only defined in fully gapped bands. Furthermore, due to the spin-momentum locking of the non-driven system, the pseudospin texture induced by the drive is non-trivial, contributing 1/2 to the band's Chern number. In addition, the gap opening at $\mathbf{k} = \mathbf{K}$, aligns the pseudospin in the z -direction, see Figure 12c.

The off-resonant process can be intuitively understood as the emission and reabsorption of the drive photon, which corresponds to a second-order effect in the electrons-drive cou-

pling. Mathematically, the gap opening can be understood by an effective Hamiltonian written in the basis of $|\psi_{CB}(\mathbf{K})\rangle$, and $|\psi_{VB}(\mathbf{K})\rangle$, evaluated at $\mathbf{k} = \mathbf{K}$. This Hamiltonian has the same form as in Equation (12), yet with the off-diagonal term given by^[192] $V_{OR} = \langle \psi_{CB}(\mathbf{K}) | \frac{1}{\hbar\Omega} [H^{(1)}(\mathbf{K}), H^{(-1)}(\mathbf{K})] | \psi_{VB}(\mathbf{K}) \rangle$ (Recall the definition of $H^{(m)}(\mathbf{k})$ below Equation (12)). The contribution to the Chern number from the \mathbf{K}' point, leads to the same value of 1/2, giving rise to a total contribution of one from both valleys.

4.2.4. Dynamical Topological Transition in a Resonantly Driven Graphene Sheet

Both resonant and off-resonant topological transitions come into play in graphene driven by circularly polarized light in the MIR range.^[147,193,194] The topological Floquet bands give rise to topological edge states at the edges of the system. **Figure 13a** shows the band-structure of graphene driven by a circularly polarized light on a strip with zigzag edges, projected on the momentum k_{\parallel} along the strip. The intensity indicates the time-averaged density of states, with bands of lower intensity corresponding to the Floquet sidebands. The spectrum exhibits three dynamically opened topological gaps, Δ_0 at $\varepsilon = 0$ and Δ_1 at $\varepsilon = \pm\hbar\Omega/2$ with two linearly dispersed subgap states corresponding to topological edge states localized at the opposite edges, with opposite chiralities. The branches colored red and blue denote the states localized at the same edges as indicated in the inset of this figure.

The edge states near one of the edges are related to the Chern numbers of the bulk bands by the following relation: the Chern number of a band equals the difference between the net chirality of edge states in the gap above this band, and the net chirality in the gap below it.^[161,195] For example, consider the Floquet band in the range $0 < \varepsilon < \hbar\Omega/2$ in Figure 13a. The gap

Δ_1 , lying around $\varepsilon = \hbar\Omega/2$ hosts two edge states with right chirality on the right edge of the sample. In turn, the gap Δ_0 , lying around $\varepsilon = 0$, hosts a single edge with left chirality on the right edge of the sample. Using the formula above, we obtain the Chern number of the corresponding Floquet band yielding $C = 3$, for each physical spin. This value agrees with Sections 4.2.2 and 4.2.3, where we concluded that each valley contributed one to the Chern number from the resonant transitions and another 1/2 from the off-resonant transitions. A total contribution from both K and K' valleys amounts to $C = 3$.

Signatures of the induced non-trivial topology of driven graphene were observed in a time-resolved transport experiment by McIver et al.^[167] In this experiment, 1L graphene was illuminated by a circularly polarized light with a frequency of 46 THz and peak electric field strength of 4×10^7 V m⁻¹. For these parameters, the induced gap at the Dirac point is estimated by $\Delta_0 \approx 69$ meV and the resonant gap is estimated by $\Delta_1 \approx 56$ meV, see Figure 13b.

The system is probed by an ultra-fast transport measurement of the Hall conductance (G_{xy}) in a four-probe measurement geometry. The Hall conductance showed a plateau with a width of ≈ 60 meV, where $G_{xy} = (1.8 \pm 0.4)e^2/h$ when the chemical potential is tuned close to the Dirac point, see Figure 13b, right panel. The transport measurement of Hall conductance provides indirect evidence of the band topology in the system.^[145,196–199] The signal consists of contributions of the bulk and the topological edge states,^[200,201] where the bulk contribution arises from the Berry curvature (see Equation (11)) of the occupied states.

To fully appreciate this result, a better understanding of the electronic distribution is needed. Recent theoretical works have obtained electronic distributions in graphene, based on phenomenological models of electron relaxation rates, giving rise to a transport signal that agrees with the experimental

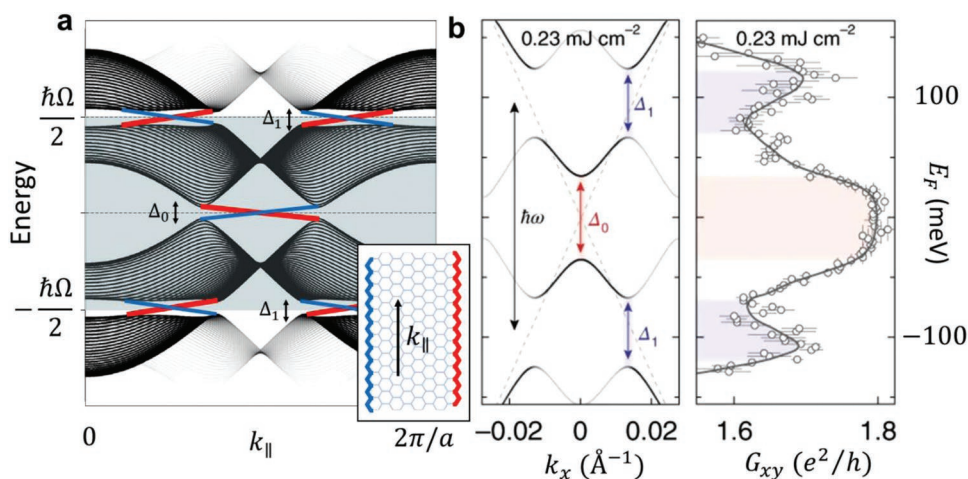


Figure 13. Graphene driven by a circularly polarized light. a) Numerically calculated band-structure of a periodically driven graphene defined on a strip with zigzag edges (as shown off-scale in the inset), projected on the momentum parallel to the strip, k_{\parallel} . The intensity indicates the period-averaged density of states. The spectrum exhibits resonant Floquet gaps at $\varepsilon = \pm\hbar\Omega/2$ and an off-resonant gap at $\varepsilon = 0$. The in-gap states with a linear dispersion indicate edge states localized at the two edges of the strip, where the red- and blue-colored states are localized at the right and left edges, respectively, as indicated in the inset by the same colors. Reproduced with permission.^[140] Copyright 2020, Nature Publishing Group. b) The theoretical spectrum (left) and measured anomalous conductivity G_{xy} as a function of the filling E_F (right), in graphene illuminated by the circularly polarized light. The anomalous conductivity exhibits approximate plateaus when the filling corresponds to the full Floquet bands (it is more pronounced in the central plateau for $E_F = 0$). Reproduced with permission.^[167] Copyright 2020, Nature Publishing Group.

results.^[202–204] Going beyond this demonstration of the topological character of the bands, it is desired to gain a direct measure of the Floquet bands, their topological character, and their subsequent edge effects. The induced topology of the bulk bands can be performed by measuring circular dichroism of the spectroscopic signal.^[205,206] This challenging quest in 2D materials has the potential to thrive with the development of multi-dimensional TR-ToF-MM, as discussed in the following.

4.3. Probing Floquet Band-Topologies with Multi-Dimensional TR-MM

The direct observation of the Floquet band-structure, its population, and its topological character in a 2D sample and its edges can supply unequivocal evidence for the coherent band engineering, unmasked by any additional process that is manifested by it. Indeed, TR-ARPES has been used to visualize the effect of Floquet engineering of the surface band-structure of a 3D topological insulator,^[103] or a dense ensemble of one-dimensional edge states over the top surface of a Bismuthene, a layered equilibrium topological insulator.^[207] However, capturing the one-dimensional edge states in a 2D sample is more challenging, as it requires nanometric spatial resolutions to separate the edge states signals from the bulk band-structure. For example, scanning probe techniques with high-spatial resolutions have been used to image the presence of one-dimensional edge states at the edges of 1L WTe₂, a topological insulator in equilibrium.^[33] Therefore, obtaining momentum-space insight into Floquet band engineering and its topology would gain significantly by the simultaneous resolution of several dimensions of the studied electronic structures. It is a natural fit with the opportunities offered by SR-TR-ToF-MM, as follows.

First, the driven nature of the Floquet bands requires pulsed excitations, allowing to effectively drive the material with strong fields for short times to not damage them. Thus, it naturally requires a temporal resolution of the order of tens of femtoseconds, enabling probing of the structure while it is being driven.

Second, the microscopic scale of high-quality monolayered flakes, and more so the nanometric widths of the domain of the topological edge states require fine spatial resolution. This can be achieved either in the TR-PEEM mode of the M or by otherwise clever filtering (using dark-field MM) of the edge states from the overwhelming bulk band-structure.

Third, the 2D image that is captured by the ToF detector is essential for full visualization of the momentum-space character of the edge states in the 2D BZ. Floquet band-crossings, hybridizations of band replica, and the edge modes, may not lie on specific high-symmetry axes of the BZ and are expected to span over more than just a few points in the momentum-space. Thus, an instant 2D image of the entire BZ should acquire the signal from these effects more efficiently than a single dimension of characterization (as in ARPES and its variants).

Fourth, analyzing the topology of the bands calls for sensing their pseudospin textures. This, in many cases, involves mapping the spin texture of the bands. Once again, the facile combination of spin-filtering into SR-TR-ToF-MM is advantageous for this task. On top of that, the ability to control the drive field circular polarization is essential for controlling the valley degree

of freedom in 2D materials or observing the Berry curvature^[205] of the Floquet bands.

4.4. Perspectives on Floquet Engineering

Floquet engineering of vdW materials expands beyond band topology.^[141–143] It can be used to control the optical properties of materials and facilitate the emergence of new correlated states.^[208–213] In a recent experiment, Shan et al.^[155] has demonstrated that a periodic electric field pulse shone on manganese phosphorus trisulfide, suppressed the second-harmonic generation by about 90%. During the pulse, the second harmonic signal was suppressed and then rapidly restored once the pulse has decayed. This effect was explained by the Floquet hybridization of the atomic orbitals giving rise to unusual optical properties.

Another promising direction is moiré-Floquet engineering,^[166] in which the properties of layered materials are altered by controlling the moiré pattern that forms in artificial stacks of two or more layers^[2,155,205,214–220] (e.g., by changing the twist angle between the layers) and by controlling the Floquet spectrum by an external drive.

The central interest of the moiré-Floquet approach is the generation and dynamical control of flat bands. The drive has been shown to induce flat bands over a wide range of twist angles.^[217,218] Furthermore, circularly polarized light induces topology in the flat bands through the mechanism of off-resonant transitions,^[219] as discussed in Section 4.2.3. For example, placing a sample of twisted bilayer graphene in a waveguide can modulate interlayer hopping through Floquet engineering.^[220]

4.5. Population Dynamics, Heating, and Many-Body Effects

Floquet engineering of materials is a powerful tool, that can induce a wide range of nonequilibrium phenomena in 2D materials, by dynamically modifying the band-structure of the material. However, illumination of the material by a strong continuous drive affects also the electronic population by creating excitations (see Section 3) and inducing non-equilibrium electronic dynamics. Electronic dynamics induced by an external drive is a complex phenomenon involving electron-electron scattering, interaction with phonons, and collisions with other quasiparticles and impurities in the solid.^[221,222] These processes often result in the heating of the material and the decay of order in the system.^[223,224] Mitigation of the heating effects and controlling the many-body dynamics is thus a substantial challenge in Floquet experiments. Driving the system with a far off-resonant drive may induce a prethermal state^[225–228] in which the heating is strongly suppressed.^[192,229–231] Furthermore, coupling the system to a cold bath, for example, via acoustic phonons in semiconducting layers can slow down the heating processes and even stabilize electronic steady states in the system with exotic phase.^[232–238] Time-resolved spectroscopic techniques can be applied to image the steady states and heating dynamics in the momentum-space. A recent experiment employed the time-resolved X-ray photoelectron spectroscopy technique to probe the effective temperature of

the transiently excited hot electron gas in graphene.^[239] These results have been gained using the TR-ToF-MM at the free-electron laser FLASH.

High-resolution measurements performed using the MM technique can shed new light on the heating and cooling mechanisms in solids and help separate the effects originating from the Floquet induced spectrum and photoexcitations.

5. Desired Advances in Experimental Capabilities

Concluding this review and perspective, we bring here a roadmap for the development of MM-based instrumentation that is needed to promote the scientific agenda discussed in Sections 3.4 and 4. This is categorized into four sectors: accessing higher probe energies, improving the energy resolution of the experiment, improved control over sample temperature, and control of sample electrostatics:

5.1. Probe Energy

As mentioned earlier, photoemission pulses in the 100 eV energy range can yield rich additional information beyond that of the VB and CB structures. Reaching such energies has so far only been possible in FEL facilities. Therefore it is required to set-up of TR-ToF-MM systems in FEL facilities, as is currently being done in several locations worldwide. Such high energy experiments will nevertheless have to overcome issues of space-charge (due to the intensity of the pulses), and of energy and momentum resolution, as referred to in the next point.

5.2. Energy Resolution

As with any ARPES instrumentation, improvements in energy resolution enable one to see finer spectral features and fragile correlated states. Currently, the limits to the measured energy resolution come from sample inhomogeneity, which is likely due to sample fabrication processes. Such improvements in the sample will follow the recent improvements in energy resolution TR-ToF-MM instrumentation, that uses efficient MHz-rate XUV generation techniques with picosecond pulses, so as to not limit the energy resolution via the XUV probe pulses.^[60] We note that in such a setup, the goal would not be to study the rapid dynamics of photoexcited states, but the correlated nature of long-lived photoexcited states that have achieved quasi-equilibrium with the lattice temperatures at long time-delays after photoexcitation.

5.3. Sample Temperature

Cooling the sample to lower temperatures will serve to both improve the measured band-structure linewidths and also ensure the survival of fragile correlated states. For example, many of the electronic Wigner crystals melt at temperatures below 50 K,^[132,240] and excitonic condensed phases have also been reported in that temperature range.^[122,123] Lower

temperatures in the few Kelvin range may also access hitherto unknown physics. Achieving such low sample temperatures requires further developments in the sample stage engineering and cooling in an MM.

5.4. Sample Electrostatics

To express various condensed and correlated electronic and excitonic phases in 2D samples it is necessary to carefully control their charge density. Graphite gate electrodes or metallic contacts deposited on the sample^[241] could serve as electrostatic gates, on top of being charge reservoirs for the photoemission process. However, the geometry and structure of these gates need to be compatible with MM, where the requirements of uniformity and strength of the large extraction voltage can make this quite challenging. When accessing higher electronic kinetic energies (e.g., by using FEL sources), novel multi-mode front lens allows operating the ToF-MM with zero extractor field,^[242] such that gate electrodes required for operando studies do not deteriorate the instrument performance.

6. Summary

In this paper, we reviewed the decades-long evolution of momentum-resolved photoemission experiments, and the scientific breakthroughs they have been driving through the study of 2D, vdW, materials. Steady-state ARPES characterizes the unperturbed band-structure of solids by resolving photoemitted electrons in angle (momentum) and energy. In TR-ARPES the material is photoexcited, or driven, prior to the photoemission, such that the driven band-structure and previously unoccupied states can be studied. Alternatively, SR-ARPES and μ ARPES offer spin or spatial selectivity, respectively, of ARPES experiments. The advent of TR-ToF-MM allowed enjoying the best of all worlds, combining temporal resolution, spatial selectivity (and agile reconfiguration to PEEM), easy incorporation of spin-measurement, a complete 2D imaging of momentum-space, with enhanced repetition rates to avoid space-charge effects without compromising on signal levels.

We focused on the scientific fruits of this advancement in the context of 2D materials since their few-atoms thickness allows to directly probe their native band-structure, as opposed to bulk materials where only the surface properties are probed. Moreover, we have laid-down the benefits of using TR-ToF-MM for their study, accessing small, yet homogeneous and high-quality, samples supported by insulating substrates. Our attention was divided into two facets: the physics of excitations (excited charge-carriers and excitons) in 2D materials, and complementarily the physics of the driven, but not excited, band-structure, leading to Floquet band engineering.

Surveying the work on excited state characterization, we found many TR-ARPES studies of the dynamics of electrons in the CB of 2D semiconductors like TMDCs and graphene, showing various processes of scattering from one valley to another, charge-transfer, etc. Employing TR-ToF-MM, alongside improvements in the sample quality, allowed to see, for

the first time, excitonic signatures in momentum-space, which were so far inaccessible along decades of their optical exploration. It then allowed exploring their wavefunction characteristics and their dynamics. The characteristic theoretical and experimental fingerprints of an excitonic state in momentum-space are described as well, highlighting the advantages of this momentum-space viewpoint on excitons compared with the more traditional optical spectroscopy. Furthermore, we discuss the ongoing effort to characterize the wavefunctions of a variety of excitonic states in 2D materials, and the impact of exciton–exciton and exciton–charge interactions on them. Following up on this line of research, we envision the possibilities of exploring the photoexcitation-induced dynamics of more exotic states, where many excitons and charge-carriers participate in highly correlated phases.

As an alternative route for light-driven modifications in the material properties, we turn to cover the facet of Floquet band engineering, that is, tuning the band-structure and creating new material properties using an oscillating light field. One important example is altering the band-topology and the creation of electronic edge states by closing the bandgap of the material with the Floquet replica of the original bands. We discuss the possibilities of examining these effects in 2D materials using TR-ToF-MM and compare that to existing evidence for edge-state emergence. We dwell upon the opportunities of combining moiré band-engineering with Floquet engineering. We finish this section discussing the combination of Floquet band engineering with photoexcited populations of charges and excitons, from many-body interactions, through heating of the sample and electron(exciton)–phonon interactions, etc.

Finally, we equip the research outlook with the desired experimental TR-ToF-MM improvements we envision as cardinal for its execution.

Overall, we conclude that the improvements in instrumentation and samples created a wide range of opportunities in the study of 2D materials band-structure, excited states, and driven phenomena, that can yield not only the fundamental physical knowledge about these systems, but also many applications of 2D materials in quantum computation, photonics, and electronics.

Acknowledgements

O.K. thanks the funding from the Koret Foundation, the AMOS program, Chemical Sciences, Geosciences, and Biosciences Division, Basic Energy Sciences, U.S. Department of Energy, and the Gordon and Betty Moore Foundation's EPIQS Initiative through grant number GBMF9462. I.E. is grateful for the support from the Simons Foundation. K.M.D. thanks the funding from the Femtosecond Spectroscopy Unit—Okinawa Institute of Science and Technology Graduate University, and the Okinawa Institute of Science and Technology Graduate University Innovative Technology Research—Proof of Concept Program.

Conflict of Interest

K.M.D. is an inventor on a patent application related to this work filed by the Okinawa Institute of Science and Technology School Corporation (US 2020/0333559 A1 published on October 22, 2020).

Keywords

2D materials, angle-resolved photoemission spectroscopy, band-structure characterization, excitons, Floquet bands engineering, time-resolved momentum-microscopy, topological edge states

Received: May 6, 2022

Revised: June 23, 2022

Published online:

- [1] P. Ajayan, P. Kim, K. Banerjee, *Phys. Today* **2016**, 69, 38.
- [2] D. M. Kennes, M. Claassen, L. Xian, A. Georges, A. J. Millis, J. Hone, C. R. Dean, D. N. Basov, A. N. Pasupathy, A. Rubio, *Nat. Phys.* **2021**, 17, 155.
- [3] X. Liu, M. C. Hersam, *Nat. Rev. Mater.* **2019**, 4, 669.
- [4] D. B. Sulas-Kern, E. M. Miller, J. L. Blackburn, *Energy Environ. Sci.* **2020**, 13, 2684.
- [5] J. Deslippe, G. Samsonidze, D. A. Strubbe, M. Jain, M. L. Cohen, S. G. Louie, *Comput. Phys. Commun.* **2012**, 183, 1269.
- [6] A. Chernikov, T. C. Berkelbach, H. M. Hill, A. Rigosi, Y. Li, O. B. Aslan, D. R. Reichman, M. S. Hybertsen, T. F. Heinz, *Phys. Rev. Lett.* **2014**, 113, 076802.
- [7] X.-X. Zhang, Y. You, S. Y. F. Zhao, T. F. Heinz, *Phys. Rev. Lett.* **2015**, 115, 257403.
- [8] E. Malic, M. Selig, M. Feierabend, S. Brem, D. Christiansen, F. Wendler, A. Knorr, G. Berghäuser, *Phys. Rev. Mater.* **2018**, 2, 014002.
- [9] E. Courtade, M. Semina, M. Manca, M. M. Glazov, C. Robert, F. Cadiz, G. Wang, T. Taniguchi, K. Watanabe, M. Pierre, W. Escoffier, E. L. Ivchenko, P. Renucci, X. Marie, T. Amand, B. Urbaszek, *Phys. Rev. B* **2017**, 96, 085302.
- [10] A. K. Geim, I. V. Grigorieva, *Nature* **2013**, 499, 419.
- [11] B. Amin, N. Singh, U. Schwingenschlög, *Phys. Rev. B* **2015**, 92, 075439.
- [12] C. Zhang, C. Gong, Y. Nie, K.-A. Min, C. Liang, Y. J. Oh, H. Zhang, W. Wang, S. Hong, L. Colombo, R. M. Wallace, K. Cho, *2D Mater.* **2017**, 4, 015026.
- [13] R. Gillen, J. Maultzsch, *Phys. Rev. B* **2018**, 97, 165306.
- [14] D. A. Ruiz-Tijerina, V. I. Fal'ko, *Phys. Rev. B* **2019**, 99, 125424.
- [15] A. Raja, A. Chaves, J. Yu, G. Arefe, H. M. Hill, A. F. Rigosi, T. C. Berkelbach, P. Nagler, C. Schüller, T. Korn, C. Nuckolls, J. Hone, L. E. Brus, T. F. Heinz, D. R. Reichman, A. Chernikov, *Nat. Commun.* **2017**, 8, 15251.
- [16] P. Rivera, H. Yu, K. L. Seyler, N. P. Wilson, W. Yao, X. Xu, *Nat. Nanotechnol.* **2018**, 13, 1004.
- [17] H. Yu, G.-B. Liu, J. Tang, X. Xu, W. Yao, *Sci. Adv.* **2017**, 3, e1701696.
- [18] F. Wu, T. Lovorn, E. Tutuc, A. H. MacDonald, *Phys. Rev. Lett.* **2018**, 121, 026402.
- [19] E. M. Alexeev, D. A. Ruiz-Tijerina, M. Danovich, M. J. Hamer, D. J. Terry, P. K. Nayak, S. Ahn, S. Pak, J. Lee, J. I. Sohn, M. R. Molas, M. Koperski, K. Watanabe, T. Taniguchi, K. S. Novoselov, R. V. Gorbachev, H. S. Shin, V. I. Fal'ko, A. I. Tartakovskii, *Nature* **2019**, 567, 81.
- [20] H. Pan, F. Wu, S. D. Sarma, *Phys. Rev. Res.* **2020**, 2, 033087.
- [21] Y. Cao, V. Fatemi, S. Fang, K. Watanabe, T. Taniguchi, E. Kaxiras, P. Jarillo-Herrero, *Nature* **2018**, 556, 43.
- [22] A. L. Sharpe, E. J. Fox, A. W. Barnard, J. Finney, K. Watanabe, T. Taniguchi, M. A. Kastner, D. Goldhaber-Gordon, *Science* **2019**, 365, 605.
- [23] G. Chen, A. L. Sharpe, P. Gallagher, I. T. Rosen, E. J. Fox, L. Jiang, B. Lyu, H. Li, K. Watanabe, T. Taniguchi, J. Jung, Z. Shi, D. Goldhaber-Gordon, Y. Zhang, F. Wang, *Nature* **2019**, 572, 215.

- [24] H. C. Po, L. Zou, A. Vishwanath, T. Senthil, *Phys. Rev. X* **2018**, *8*, 031089.
- [25] L. Wang, E.-M. Shih, A. Ghiotto, L. Xian, D. A. Rhodes, C. Tan, M. Claassen, D. M. Kennes, Y. Bai, B. Kim, K. Watanabe, T. Taniguchi, X. Zhu, J. Hone, A. Rubio, A. N. Pasupathy, C. R. Dean, *Nat. Mater.* **2020**, *19*, 861.
- [26] Y. Tang, L. Li, T. Li, Y. Xu, S. Liu, K. Barmak, K. Watanabe, T. Taniguchi, A. H. MacDonald, J. Shan, K. F. Mak, *Nature* **2020**, *579*, 353.
- [27] E. C. Regan, D. Wang, C. Jin, M. I. Bakti Utama, B. Gao, X. Wei, S. Zhao, W. Zhao, Z. Zhang, K. Yumigeta, M. Blei, J. D. Carlström, K. Watanabe, T. Taniguchi, S. Tongay, M. Crommie, A. Zettl, F. Wang, *Nature* **2020**, *579*, 359.
- [28] F. Wu, T. Lovorn, A. H. MacDonald, *Phys. Rev. B* **2018**, *97*, 035306.
- [29] F. Wu, T. Lovorn, A. H. MacDonald, *Phys. Rev. Lett.* **2017**, *118*, 147401.
- [30] T. Li, S. Jiang, B. Shen, Y. Zhang, L. Li, Z. Tao, T. Devakul, K. Watanabe, T. Taniguchi, L. Fu, J. Shan, K. F. Mak, *Nature* **2021**, *600*, 641.
- [31] X. Xu, W. Yao, D. Xiao, T. F. Heinz, *Nat. Phys.* **2014**, *10*, 343.
- [32] X. Qian, J. Liu, L. Fu, J. Li, *Science* **2014**, *346*, 1344.
- [33] G. Schönhense, K. Medjanik, H.-J. Elmers, *J. Electron Spectrosc. Relat. Phenom.* **2015**, *200*, 94.
- [34] J. A. Sobota, Y. He, Z.-X. Shen, *Rev. Mod. Phys.* **2021**, *93*, 025006.
- [35] B. Lv, T. Qian, H. Ding, *Nat. Rev. Phys.* **2019**, *1*, 609.
- [36] M. Cattelan, N. A. Fox, *Nanomaterials* **2018**, *8*, 284.
- [37] A. Grubišić Čabo, J. A. Miwa, S. S. Grønberg, J. M. Riley, J. C. Johannsen, C. Cacho, O. Alexander, R. T. Chapman, E. Springate, M. Griioni, J. V. Lauritsen, P. D. C. King, P. Hofmann, S. Ulstrup, *Nano Lett.* **2015**, *15*, 5883.
- [38] F. de Groot, A. Kotani, *Core Level Spectroscopy of Solids*, CRC Press, Boca Raton, FL **2008**.
- [39] M. Dendzik, R. P. Xian, E. Perfetto, D. Sangalli, D. Kutnyakhov, S. Dong, S. Beaulieu, T. Pincelli, F. Pressacco, D. Curcio, S. Y. Agustsson, M. Heber, J. Hauer, W. Wurth, G. Brenner, Y. Acremann, P. Hofmann, M. Wolf, A. Marini, G. Stefanucci, L. Rettig, R. Ernstorfer, *Phys. Rev. Lett.* **2020**, *125*, 096401.
- [40] K. Baumgärtner, M. Reuner, C. Metzger, D. Kutnyakhov, M. Heber, F. Pressacco, C.-H. Min, T. R. F. Peixoto, M. Reiser, C. Kim, W. Lu, R. Shayduk, M. Izquierdo, G. Brenner, F. Roth, A. Schöll, S. Molodtsov, W. Wurth, F. Reinert, A. Madsen, D. Popova-Gorelova, M. Scholz, *Nat. Commun.* **2022**, *13*, 2741.
- [41] P. Puschnig, D. Lüftner, *J. Electron Spectrosc. Relat. Phenom.* **2015**, *200*, 193.
- [42] L. X. Yang, B. P. Xie, Y. Zhang, C. He, Q. Q. Ge, X. F. Wang, X. H. Chen, M. Arita, J. Jiang, K. Shimada, M. Taniguchi, I. Vobornik, G. Rossi, J. P. Hu, D. H. Lu, Z. X. Shen, Z. Y. Lu, D. L. Feng, *Phys. Rev. B* **2010**, *82*, 104519.
- [43] J. D. Koralek, J. F. Douglas, N. C. Plumb, Z. Sun, A. V. Fedorov, M. M. Murnane, H. C. Kapteyn, S. T. Cundiff, Y. Aiura, K. Oka, H. Eisaki, D. S. Dessau, *Phys. Rev. Lett.* **2006**, *96*, 017005.
- [44] Y. He, I. M. Vishik, M. Yi, S. Yang, Z. Liu, J. J. Lee, S. Chen, S. N. Rebec, D. Leuenberger, A. Zong, C. M. Jefferson, R. G. Moore, P. S. Kirchmann, A. J. Merriam, Z.-X. Shen, *Rev. Sci. Instrum.* **2016**, *87*, 011301.
- [45] Z. Huang, K.-J. Kim, *Phys. Rev. Spec. Top.-Accel. Beams* **2007**, *10*, 034801.
- [46] F. Pressacco, D. Sangalli, V. Uhlř, D. Kutnyakhov, J. A. Arregi, S. Y. Agustsson, G. Brenner, H. Redlin, M. Heber, D. Vasilyev, J. Demsar, G. Schönhense, M. Gatti, A. Marini, W. Wurth, F. Sirotti, *Nat. Commun.* **2021**, *12*, 5088.
- [47] L.-P. Oloff, M. Oura, K. Rossnagel, A. Chainani, M. Matsunami, R. Eguchi, T. Kiss, Y. Nakatani, T. Yamaguchi, J. Miyawaki, M. Taguchi, K. Yamagami, T. Togashi, T. Katayama, K. Ogawa, M. Yabashi, T. Ishikawa, *New J. Phys.* **2014**, *16*, 123045.
- [48] J. Maklar, S. Dong, S. Beaulieu, T. Pincelli, M. Dendzik, Y. W. Windsor, R. P. Xian, M. Wolf, R. Ernstorfer, L. Rettig, *Rev. Sci. Instrum.* **2020**, *91*, 123112.
- [49] R. P. Day, I. S. Elfimov, A. Damascelli, (Preprint) *ArXiv: 2109.13274* **2021**.
- [50] S.-K. Mo, C. Hwang, Y. Zhang, M. Fanciulli, S. Muff, J. H. Dil, Z.-X. Shen, Z. Hussain, *J. Phys. Condens. Matter* **2016**, *28*, 454001.
- [51] C. Tusche, A. Krasnyuk, J. Kirschner, *Ultramicroscopy* **2015**, *159*, 520.
- [52] D. Kutnyakhov, R. P. Xian, M. Dendzik, M. Heber, F. Pressacco, S. Y. Agustsson, L. Wenthaus, H. Meyer, S. Gieschen, G. Mercurio, A. Benz, K. Bühlman, S. Däster, R. Gort, D. Curcio, K. Volckaert, M. Bianchi, C.h. Sanders, J. A. Miwa, S. Ulstrup, A. Oelsner, C. Tusche, Y.-J. Chen, D. Vasilyev, K. Medjanik, G. Brenner, S. Dziarzhyski, H. Redlin, B. Manschwetus, S. Dong, et al., *Rev. Sci. Instrum.* **2020**, *91*, 013109.
- [53] H. Carstens, M. Högner, T. Saule, S. Holzberger, N. Lilienfein, A. Guggenmos, C. Jocher, T. Eidam, D. Esser, V. Tosa, V. Pervak, J. Limpert, A. Tünnermann, U. Kleineberg, F. Krausz, I. Pupeza, *Optica* **2016**, *3*, 366.
- [54] N. Kanda, T. Imahoko, K. Yoshida, A. Tanabashi, A. Amani Eilanlou, Y. Nabekawa, T. Sumiyoshi, M. Kuwata-Gonokami, K. Midorikawa, *Light: Sci. Appl.* **2020**, *9*, 168.
- [55] R. Klas, A. Kirsche, M. Gebhardt, J. Buldt, H. Stark, S. Hädrich, J. Rothhardt, J. Limpert, *Photonix* **2021**, *2*, 4.
- [56] M. Kotsugi, W. Kuch, F. Offi, L. I. Chelaru, J. Kirschner, *Rev. Sci. Instrum.* **2003**, *74*, 2754.
- [57] G. Schönhense, H.-J. Elmers, *J. Vac. Sci. Technol., A* **2022**, *40*, 020802.
- [58] B. Krömker, M. Escher, D. Funnemann, D. Hartung, H. Engelhard, J. Kirschner, *Rev. Sci. Instrum.* **2008**, *79*, 053702.
- [59] K. Medjanik, O. Fedchenko, S. Chernov, D. Kutnyakhov, M. Ellguth, A. Oelsner, B. Schönhense, T. R. F. Peixoto, P. Lutz, C.-H. Min, F. Reinert, S. Däster, Y. Acremann, J. Vieffhaus, W. Wurth, H. J. Elmers, G. Schönhense, *Nat. Mater.* **2017**, *16*, 615.
- [60] G. Schönhense, K. Medjanik, O. Fedchenko, A. Zymaková, S. Chernov, D. Kutnyakhov, D. Vasilyev, S. Babenkov, H. J. Elmers, P. Baumgärtel, P. Goslawski, G. Öhrwall, T. Grunke, T. Kauerhof, K. von Volkmann, M. Kallmayer, M. Ellguth, A. Oelsner, *J. Synchrotron Radiat.* **2021**, *28*, 1891.
- [61] S. Chernov, C. Lidig, O. Fedchenko, K. Medjanik, S. Babenkov, D. Vasilyev, M. Jourdan, G. Schönhense, H. J. Elmers, *Phys. Rev. B* **2021**, *103*, 054407.
- [62] S. Shabani, D. Halbertal, W. Wu, M. Chen, S. Liu, J. Hone, W. Yao, D. N. Basov, X. Zhu, A. N. Pasupathy, *Nat. Phys.* **2021**, *17*, 720.
- [63] H. Li, S. Li, M. H. Naik, J. Xie, X. Li, J. Wang, E. Regan, D. Wang, W. Zhao, S. Zhao, S. Kahn, K. Yumigeta, M. Blei, T. Taniguchi, K. Watanabe, S. Tongay, A. Zettl, S. G. Louie, F. Wang, M. F. Crommie, *Nat. Mater.* **2021**, *20*, 945.
- [64] D. Pommier, R. Bretel, L. E. P. López, F. Fabre, A. Mayne, E. Boer-Duchemin, G. Dujardin, G. Schull, S. Berciaud, E. L. e Moal, *Phys. Rev. Lett.* **2019**, *123*, 027402.
- [65] G. Berghäuser, P. Steinleitner, P. Merkl, R. Huber, A. Knorr, E. Malic, *Phys. Rev. B* **2018**, *98*, 020301.
- [66] X.-X. Zhang, T. Cao, Z. Lu, Y.-C. Lin, F. Zhang, Y. Wang, Z. Li, J. C. Hone, J. A. Robinson, D. Smirnov, S. G. Louie, T. F. Heinz, *Nat. Nanotechnol.* **2017**, *12*, 883.
- [67] Z. Lu, D. Rhodes, Z. Li, D. V. Tuan, Y. Jiang, J. Ludwig, Z. Jiang, Z. Lian, S.-F. Shi, J. Hone, H. Dery, D. Smirnov, *2D Mater.* **2019**, *7*, 015017.
- [68] G. Wang, C. Robert, M. M. Glazov, F. Cadiz, E. Courtade, T. Amand, D. Lagarde, T. Taniguchi, K. Watanabe, B. Urbaszek, X. Marie, *Phys. Rev. Lett.* **2017**, *119*, 047401.
- [69] C. Jin, E. Y. Ma, O. Karni, E. C. Regan, F. Wang, T. F. Heinz, *Nat. Nanotechnol.* **2018**, *13*, 994.

- [70] P. Merkl, F. Mooshammer, P. Steinleitner, A. Girnglhuber, K.-Q. Lin, P. Nagler, J. Holler, C. Schüller, J. M. Lupton, T. Korn, S. Ovesen, S. Brem, E. Malic, R. Huber, *Nat. Mater.* **2019**, *18*, 691.
- [71] D. Sun, Y. Rao, G. A. Reider, G. Chen, Y. You, L. Brézin, A. R. Harutyunyan, T. F. Heinz, *Nano Lett.* **2014**, *14*, 5625.
- [72] V. Pareek, J. Madéo, K. M. Dani, *Phys. Rev. Lett.* **2020**, *124*, 057403.
- [73] D. Erckensten, S. Brem, E. Malic, *Phys. Rev. B* **2021**, *103*, 045426.
- [74] J. C. Johannsen, S. Ulstrup, F. Cilento, A. Crepaldi, M. Zacchigna, C. Cacho, I. C. E. Turcu, E. Springate, F. Fromm, C. Raidel, T. Seyller, F. Parmigiani, M. Grioni, P. Hofmann, *Phys. Rev. Lett.* **2013**, *111*, 027403.
- [75] S. Aeschlimann, R. Krause, M. Chávez-Cervantes, H. Bromberger, R. Jago, E. Malić, A. Al-Temimy, C. Coletti, A. Cavalleri, I. Gierz, *Phys. Rev. B* **2017**, *96*, 020301.
- [76] S. Ulstrup, J. C. Johannsen, F. Cilento, A. Crepaldi, J. A. Miwa, M. Zacchigna, C. Cacho, R. T. Chapman, E. Springate, F. Fromm, C. Raidel, T. Seyller, P. D. C. King, F. Parmigiani, M. Grioni, P. Hofmann, *J. Electron Spectrosc. Relat. Phenom.* **2015**, *200*, 340.
- [77] R. Wallauer, J. Reimann, N. Armbrust, J. Gütde, U. Höfer, *Appl. Phys. Lett.* **2016**, *109*, 162102.
- [78] R. Wallauer, P. Maruhn, J. Reimann, S. Zoerb, F. Kraus, J. Gütde, M. Rohlfing, U. Höfer, *Phys. Rev. B* **2020**, *102*, 125417.
- [79] P. Hein, A. Stange, K. Hanff, L. X. Yang, G. Rohde, K. Rossnagel, M. Bauer, *Phys. Rev. B* **2016**, *94*, 205406.
- [80] M. Puppín, C. W. Nicholson, C. Monney, Y. Deng, R. P. Xian, J. Feldl, S. Dong, A. Dominguez, H. Hübener, A. Rubio, M. Wolf, L. Rettig, R. Ernstorfer, *Phys. Rev. B* **2022**, *105*, 075417.
- [81] P. Majchrzak, K. Volckaert, A. G. Čabo, D. Biswas, M. Bianchi, S. K. Mahatha, M. Dendzik, F. Andreatta, S. S. Grønberg, I. Marković, J. M. Riley, J. C. Johannsen, D. Lizzit, L. Bignardi, S. Lizzit, C. Cacho, O. Alexander, D. Matselyukh, A. S. Wyatt, R. T. Chapman, E. Springate, J. V. Lauritsen, P. D. C. King, C. E. Sanders, J. A. Miwa, P. Hofmann, S. Ulstrup, *J. Electron Spectrosc. Relat. Phenom.* **2021**, *250*, 147093.
- [82] W. Lee, Y. Lin, L.-S. Lu, W.-C. Chueh, M. Liu, X. Li, W.-H. Chang, R. A. Kaindl, C.-K. Shih, *Nano Lett.* **2021**, *21*, 7363.
- [83] S. Ulstrup, A. G. Čabo, D. Biswas, J. M. Riley, M. Dendzik, C. E. Sanders, M. Bianchi, C. Cacho, D. Matselyukh, R. T. Chapman, E. Springate, P. D. C. King, J. A. Miwa, P. Hofmann, *Phys. Rev. B* **2017**, *95*, 041405.
- [84] H. Beyer, G. Rohde, A. Grubišić Čabo, A. Stange, T. Jacobsen, L. Bignardi, D. Lizzit, P. Lacovig, C. E. Sanders, S. Lizzit, K. Rossnagel, P. Hofmann, M. Bauer, *Phys. Rev. Lett.* **2019**, *123*, 236802.
- [85] R. Bertoni, C. W. Nicholson, L. Waldecker, H. Hübener, C. Monney, U. De Giovannini, M. Puppín, M. Hoesch, E. Springate, R. T. Chapman, C. Cacho, M. Wolf, A. Rubio, R. Ernstorfer, *Phys. Rev. Lett.* **2016**, *117*, 277201.
- [86] F. Liu, Q. Li, X.-Y. Zhu, *Phys. Rev. B* **2020**, *101*, 201405.
- [87] S. Aeschlimann, A. Rossi, M. Chávez-Cervantes, R. Krause, B. Arnoldi, B. Stadtmüller, M. Aeschlimann, S. Forti, F. Fabbri, C. Coletti, I. Gierz, *Sci. Adv.* **2020**, *6*, eaay0761.
- [88] S. Dong, S. Beaulieu, M. Selig, P. Rosenzweig, D. Christiansen, T. Pincelli, M. Dendzik, J. D. Ziegler, J. Maklar, R. P. Xian, A. Neef, A. Mohammed, A. Schulz, M. Stadler, M. Jetter, P. Michler, T. Taniguchi, K. Watanabe, H. Takagi, U. Starke, A. Chernikov, M. Wolf, H. Nakamura, A. Knorr, L. Rettig, R. Ernstorfer, (*Preprint*) *ArXiv: 2108.06803*, **2021**.
- [89] H. Zhu, J. Wang, Z. Gong, Y. D. Kim, J. Hone, X.-Y. Zhu, *Nano Lett.* **2017**, *17*, 3591.
- [90] J. E. Zimmermann, M. Axt, F. Mooshammer, P. Nagler, C. Schüller, T. Korn, U. Höfer, G. Mette, *ACS Nano* **2021**, *15*, 14725.
- [91] F. Liu, M. E. Ziffer, K. R. Hansen, J. Wang, X. Zhu, *Phys. Rev. Lett.* **2019**, *122*, 246803.
- [92] S. Ulstrup, A. G. Čabo, J. A. Miwa, J. M. Riley, S. S. Grønberg, J. C. Johannsen, C. Cacho, O. Alexander, R. T. Chapman, E. Springate, M. Bianchi, M. Dendzik, J. V. Lauritsen, P. D. C. King, P. Hofmann, *ACS Nano* **2016**, *10*, 6315.
- [93] D. Biswas, A. J. H. Jones, P. Majchrzak, B. K. Choi, T.-H. Lee, K. Volckaert, J. Feng, I. Marković, F. Andreatta, C.-J. Kang, H. J. Kim, I. H. Lee, C. Jozwiak, E. Rotenberg, A. Bostwick, C. E. Sanders, Y. Zhang, G. Karras, R. T. Chapman, A. S. Wyatt, E. Springate, J. A. Miwa, P. Hofmann, P. D. C. King, Y. J. Chang, N. Lanatà, S. Ulstrup, *Nano Lett.* **2021**, *21*, 1968.
- [94] S. Beaulieu, S. Dong, N. Tancogne-Dejean, M. Dendzik, T. Pincelli, J. Maklar, R. P. Xian, M. A. Sentef, M. Wolf, A. Rubio, L. Rettig, R. Ernstorfer, *Sci. Adv.* **2021**, *7*, eabd9275.
- [95] T. Rohwer, S. Hellmann, M. Wiesenmayer, C. Sohr, A. Stange, B. Slomski, A. Carr, Y. Liu, L. M. Avila, M. Kalläne, S. Mathias, L. Kipp, K. Rossnagel, M. Bauer, *Nature* **2011**, *471*, 490.
- [96] J. Maklar, Y. W. Windsor, C. W. Nicholson, M. Puppín, P. Walmsley, V. Esposito, M. Porer, J. Rittmann, D. Leuenberger, M. Kubli, M. Savoini, E. Abreu, S. L. Johnson, P. Beaud, G. Ingold, U. Staub, I. R. Fisher, R. Ernstorfer, M. Wolf, L. Rettig, *Nat. Commun.* **2021**, *12*, 2499.
- [97] E. Perfetto, D. Sangalli, A. Marini, G. Stefanucci, *Phys. Rev. B* **2016**, *94*, 245303.
- [98] A. Steinhoff, M. Florian, M. Rösner, G. Schönhoff, T. O. Wehling, F. Jahnke, *Nat. Commun.* **2017**, *8*, 1166.
- [99] A. Rustagi, A. F. Kemper, *Phys. Rev. B* **2018**, *97*, 235310.
- [100] H. Ohnishi, N. Tomita, K. Nasu, *Int. J. Mod. Phys. B* **2017**, *32*, 1850094.
- [101] D. Christiansen, M. Selig, E. Malic, R. Ernstorfer, A. Knorr, *Phys. Rev. B* **2019**, *100*, 205401.
- [102] B. Schönhense, K. Medjanik, O. Fedchenko, S. Chernov, M. Ellguth, D. Vasilyev, A. Oelsner, J. Viehhaus, D. Kutnyakhov, W. Wurth, H. J. Elmers, G. Schönhense, *New J. Phys.* **2018**, *20*, 033004.
- [103] F. Mahmood, C.-K. Chan, Z. Alpichshev, D. Gardner, Y. Lee, P. A. Lee, N. Gedik, *Nat. Phys.* **2016**, *12*, 306.
- [104] Y. H. Wang, H. Steinberg, P. Jarillo-Herrero, N. Gedik, *Science* **2013**, *342*, 453.
- [105] K. F. Mak, C. Lee, J. Hone, J. Shan, T. F. Heinz, *Phys. Rev. Lett.* **2010**, *105*, 136805.
- [106] X. Fan, R. Nouchi, K. Tanigaki, *J. Phys. Chem. C* **2011**, *115*, 12960.
- [107] J. Madéo, M. K. L. Man, C. Sahoo, M. Campbell, V. Pareek, E. L. Wong, A. Al-Mahboob, N. S. Chan, A. Karmakar, B. M. K. Mariserla, X. Li, T. F. Heinz, T. Cao, K. M. Dani, *Science* **2020**, *370*, 1199.
- [108] M. K. L. Man, J. Madéo, C. Sahoo, K. Xie, M. Campbell, V. Pareek, A. Karmakar, E. L. Wong, A. Al-Mahboob, N. S. Chan, D. R. Bacon, X. Zhu, M. M. M. Abdelrasoul, X. Li, T. F. Heinz, F. H. da Jornada, T. Cao, K. M. Dani, *Sci. Adv.* **2021**, *7*, eabg0192.
- [109] S. Dong, M. Puppín, T. Pincelli, S. Beaulieu, D. Christiansen, H. Hübener, C. W. Nicholson, R. P. Xian, M. Dendzik, Y. Deng, Y. W. Windsor, M. Selig, E. Malic, A. Rubio, A. Knorr, M. Wolf, L. Rettig, R. Ernstorfer, *Nat. Sci.* **2021**, *1*, e10010.
- [110] R. Wallauer, R. Perea-Causin, L. Münster, S. Zajusch, S. Brem, J. Gütde, K. Tanimura, K.-Q. Lin, R. Huber, E. Malic, U. Höfer, *Nano Lett.* **2021**, *21*, 5867.
- [111] O. Karni, E. Barré, V. Pareek, J. D. Georganas, M. K. L. Man, C. Sahoo, D. R. Bacon, X. Zhu, H. B. Ribeiro, A. L. O'Beirne, J. Hu, A. Al-Mahboob, M. M. M. Abdelrasoul, N. S. Chan, A. Karmakar, A. J. Winchester, B. Kim, K. Watanabe, T. Taniguchi, K. Barmak, J. Madéo, F. H. da Jornada, T. F. Heinz, K. M. Dani, *Nature* **2022**, *603*, 247.
- [112] A. V. Stier, N. P. Wilson, K. A. Velizhanin, J. Kono, X. Xu, S. A. Crooker, *Phys. Rev. Lett.* **2018**, *120*, 057405.

- [113] A. T. Hanbicki, H.-J. Chuang, M. R. Rosenberger, C. S. Hellberg, S. V. Sivaram, K. M. McCreary, I. I. Mazin, B. T. Jonker, *ACS Nano*, **2018**, *12*, 4719.
- [114] J. Kunstmann, F. Mooshammer, P. Nagler, A. Chaves, F. Stein, N. Paradiso, G. Plechinger, C. Strunk, C. Schüller, G. Seifert, D. R. Reichman, T. Korn, *Nat. Phys.* **2018**, *14*, 801.
- [115] M. Kremser, M. Brotons-Gisbert, J. Knörzer, J. Gückelhorn, M. Meyer, M. Barbone, A. V. Stier, B. D. Gerardot, K. Müller, J. J. Finley, *npj 2D Mater. Appl.* **2020**, *4*, 8.
- [116] W. Li, X. Lu, S. Dubey, L. Devenica, A. Srivastava, *Nat. Mater.* **2020**, *19*, 624.
- [117] D. Schmitt, J. P. Bange, W. Bennecke, A. AlMutairi, K. Watanabe, T. Taniguchi, D. Steil, D. R. Luke, R. T. Weitz, S. Steil, G. S. M. Jansen, S. Hofmann, M. Reutzel, S. Mathias, *Nature* **2022**, *608*, 499.
- [118] M. Schüler, T. Pincelli, S. Dong, T. P. Devereaux, M. Wolf, L. Rettig, R. Ernstorfer, S. Beaulieu, *Phys. Rev. X* **2022**, *12*, 011019.
- [119] S. Beaulieu, J. Schusser, S. Dong, M. Schüler, T. Pincelli, M. Dendzik, J. Maklar, A. Neef, H. Ebert, K. Hricovini, M. Wolf, J. Braun, L. Rettig, J. Minár, R. Ernstorfer, *Phys. Rev. Lett.* **2020**, *125*, 216404.
- [120] S. Beaulieu, M. Schüler, J. Schusser, S. Dong, T. Pincelli, J. Maklar, A. Neef, F. Reinert, M. Wolf, L. Rettig, J. Minár, R. Ernstorfer, *npj Quantum Mater.* **2021**, *6*, 93.
- [121] Y. You, X.-X. Zhang, T. C. Berkelbach, M. S. Hybertsen, D. R. Reichman, T. F. Heinz, *Nat. Phys.* **2015**, *11*, 477.
- [122] Z. Ye, L. Waldecker, E. Y. Ma, D. Rhodes, A. Antony, B. Kim, X.-X. Zhang, M. Deng, Y. Jiang, Z. Lu, D. Smirnov, K. Watanabe, T. Taniguchi, J. Hone, T. F. Heinz, *Nat. Commun.* **2018**, *9*, 3718.
- [123] Z. Wang, D. A. Rhodes, K. Watanabe, T. Taniguchi, J. C. Hone, J. Shan, K. F. Mak, *Nature* **2019**, *574*, 76.
- [124] L. Ma, P. X. Nguyen, Z. Wang, Y. Zeng, K. Watanabe, T. Taniguchi, A. H. MacDonald, K. F. Mak, J. Shan, *Nature* **2021**, *598*, 585.
- [125] J. Wang, J. Ardelean, Y. Bai, A. Steinhoff, M. Florian, F. Jahnke, X. Xu, M. Kira, J. Hone, X.-Y. Zhu, *Sci. Adv.* **2019**, *5*, eaax0145.
- [126] A. Chernikov, C. Ruppert, H. M. Hill, A. F. Rigosi, T. F. Heinz, *Nat. Photonics* **2015**, *9*, 466.
- [127] D. Unuchek, A. Ciarrocchi, A. Avsar, K. Watanabe, T. Taniguchi, A. Kis, *Nature* **2018**, *560*, 340.
- [128] E. Liu, E. Barré, J. van Baren, M. Wilson, T. Taniguchi, K. Watanabe, Y.-T. Cui, N. M. Gabor, T. F. Heinz, Y.-C. Chang, C. H. Lui, *Nature* **2021**, *594*, 46.
- [129] B. Sun, W. Zhao, T. Palomaki, Z. Fei, E. Runburg, P. Malinowski, X. Huang, J. Cenker, Y.-T. Cui, J.-H. Chu, X. Xu, S. S. Ataei, D. Varsano, M. Palummo, E. Molinari, M. Rontani, D. H. Cobden, *Nat. Phys.* **2022**, *18*, 94.
- [130] P. Hein, S. Jauernik, H. Erk, L. Yang, Y. Qi, Y. Sun, C. Felser, M. Bauer, *J. Phys. Condens. Matter* **2020**, *32*, 345503.
- [131] D. A. Rhodes, A. Jindal, N. F. Q. Yuan, Y. Jung, A. Antony, H. Wang, B. Kim, Y. Chiu, T. Taniguchi, K. Watanabe, K. Barmak, L. Balicas, C. R. Dean, X. Qian, L. Fu, A. N. Pasupathy, J. Hone, *Nano Lett.* **2021**, *21*, 2505.
- [132] T. Smoleński, P. E. Dolgirev, C. Kuhlenkamp, A. Popert, Y. Shimazaki, P. Back, X. Lu, M. Kroner, K. Watanabe, T. Taniguchi, I. Esterlis, E. Demler, A. Imamoğlu, *Nature* **2021**, *595*, 53.
- [133] Y. Xu, S. Liu, D. A. Rhodes, K. Watanabe, T. Taniguchi, J. Hone, V. Elser, K. F. Mak, J. Shan, *Nature* **2020**, *587*, 214.
- [134] Y. Shimazaki, I. Schwartz, K. Watanabe, T. Taniguchi, M. Kroner, A. Imamoğlu, *Nature* **2020**, *580*, 472.
- [135] Y. Tang, L. Li, T. Li, Y. Xu, S. Liu, K. Barmak, K. Watanabe, T. Taniguchi, A. H. MacDonald, J. Shan, K. F. Mak, *Nature* **2020**, *579*, 353.
- [136] H. Li, S. Li, E. C. Regan, D. Wang, W. Zhao, S. Kahn, K. Yumigeta, M. Blei, T. Taniguchi, K. Watanabe, S. Tongay, A. Zettl, M. F. Crommie, F. Wang, *Nature* **2021**, *597*, 650.
- [137] X. Wang, C. Xiao, H. Park, J. Zhu, C. Wang, T. Taniguchi, K. Watanabe, J. Yan, D. Xiao, D. R. Gamelin, W. Yao, X. Xu, *Nature* **2022**, *604*, 468.
- [138] H. Pan, F. Wu, S. D. Sarma, *Phys. Rev. B* **2020**, *102*, 201104.
- [139] G. S. M. Jansen, M. Keunecke, M. Düvel, C. Möller, D. Schmitt, W. Bennecke, F. J. S. Kappert, D. Steil, D. R. Luke, S. Steil, S. Mathias, *New J. Phys.* **2020**, *22*, 063012.
- [140] R. Wallauer, M. Raths, K. Stallberg, L. Münster, D. Brandstetter, X. Yang, J. Güdde, P. Puschnig, S. Soubatch, C. Kumpf, F. C. Bocqwa, F. S. Tautz, U. Höfer, *Science* **2021**, *371*, 1056.
- [141] M. S. Rudner, N. H. Lindner, *Nat. Rev. Phys.* **2020**, *2*, 229.
- [142] T. Oka, S. Kitamura, *Annu. Rev. Condens. Matter Phys.* **2019**, *10*, 387.
- [143] C. Bao, P. Tang, D. Sun, S. Zhou, *Nat. Rev. Phys.* **2021**, *4*, 33.
- [144] A. de la Torre, D. M. Kennes, M. Claassen, S. Gerber, J. W. McIver, M. A. Sentef, *Rev. Mod. Phys.* **2021**, *93*, 041002.
- [145] D. N. Basov, R. D. Averitt, D. Hsieh, *Nat. Mater.* **2017**, *16*, 1077.
- [146] T. Kitagawa, T. Oka, A. Brataas, L. Fu, E. Demler, *Phys. Rev. B* **2011**, *84*, 235108.
- [147] N. H. Lindner, G. Refael, V. Galitski, *Nat. Phys.* **2011**, *7*, 490.
- [148] T. Oka, H. Aoki, *Phys. Rev. B* **2009**, *79*, 081406.
- [149] J. Cayssol, B. Dóra, F. Simon, R. Moessner, *Phys. Status Solidi RRL* **2013**, *7*, 101.
- [150] A. Kirilyuk, A. V. Kimel, T. Rasing, *Rev. Mod. Phys.* **2010**, *82*, 2731.
- [151] R. V. Mikhaylovskiy, E. Hendry, A. Secchi, J. H. Mentink, M. Eckstein, A. Wu, R. V. Pisarev, V. V. Kruglyak, M. I. Katsnelson, T. Rasing, A. V. Kimel, *Nat. Commun.* **2015**, *6*, 8190.
- [152] S. Chaudhary, D. Hsieh, G. Refael, *Phys. Rev. B* **2019**, *100*, 220403.
- [153] A. Sriram, M. Claassen, (*Preprint*) *ArXiv*, *ArXiv2105.01062*, (submitted, May 2021).
- [154] A. Kumar, M. Rodriguez-Vega, T. Pereg-Barnea, B. Seradjeh, *Phys. Rev. B* **2020**, *101*, 174314.
- [155] T. Morimoto, N. Nagaosa, *Sci. Adv.* **2016**, *2*, e1501524.
- [156] J.-Y. Shan, M. Ye, H. Chu, S. Lee, J.-G. Park, L. Balents, D. Hsieh, *Nature* **2021**, *600*, 235.
- [157] D. V. Else, B. Bauer, C. Nayak, *Phys. Rev. Lett.* **2016**, *117*, 090402.
- [158] D. V. Else, C. Nayak, *Phys. Rev. B* **2016**, *93*, 201103.
- [159] C. W. von Keyserlingk, S. L. Sondhi, *Phys. Rev. B* **2016**, *93*, 245146.
- [160] S. Choi, J. Choi, R. Landig, G. Kucsko, H. Zhou, J. Isoya, F. Jelezko, S. Onoda, H. Sumiya, V. Khemani, C. von Keyserlingk, N. Y. Yao, E. Demler, M. D. Lukin, *Nature* **2017**, *543*, 221.
- [161] J. Zhang, P. W. Hess, A. Kyprianidis, P. Becker, A. Lee, J. Smith, G. Pagano, I.-D. Potirniche, A. C. Potter, A. Vishwanath, N. Y. Yao, C. Monroe, *Nature* **2017**, *543*, 217.
- [162] M. S. Rudner, N. H. Lindner, E. Berg, M. Levin, *Phys. Rev. X* **2013**, *3*, 031005.
- [163] P. Titum, E. Berg, M. S. Rudner, G. Refael, N. H. Lindner, *Phys. Rev. X* **2016**, *6*, 021013.
- [164] L. J. Maczewsky, J. M. Zeuner, S. Nolte, A. Szameit, *Nat. Commun.* **2017**, *8*, 13756.
- [165] S. Mukherjee, A. Spracklen, M. Valiente, E. Andersson, P. Öhberg, N. Goldman, R. R. Thomson, *Nat. Commun.* **2017**, *8*, 13918.
- [166] F. Nathan, D. Abanin, E. Berg, N. H. Lindner, M. S. Rudner, *Phys. Rev. B* **2019**, *99*, 195133.
- [167] M. Rodriguez-Vega, M. Vogl, G. A. Fiete, *Ann. Phys.* **2021**, *435*, 168434.
- [168] J. W. McIver, B. Schulte, F.-U. Stein, T. Matsuyama, G. Jotzu, G. Meier, A. Cavalleri, *Nat. Phys.* **2020**, *16*, 38.
- [169] D. Xiao, G.-B. Liu, W. Feng, X. Xu, W. Yao, *Phys. Rev. Lett.* **2012**, *108*, 196802.
- [170] A. H. Castro Neto, F. Guinea, N. M. R. Peres, K. S. Novoselov, A. K. Geim, *Rev. Mod. Phys.* **2009**, *81*, 109.
- [171] M. Z. Hasan, C. L. Kane, *Rev. Mod. Phys.* **2010**, *82*, 3045.
- [172] X.-L. Qi, S.-C. Zhang, *Rev. Mod. Phys.* **2011**, *83*, 1057.
- [173] M. Z. Hasan, J. E. Moore, *Annu. Rev. Condens. Matter Phys.* **2011**, *2*, 55.

- [174] J. H. Shirley, *Phys. Rev.* **1965**, *138*, B979.
- [175] G. Floquet, *Ann. Sci. L'École Norm. Supér.* **1883**, *12*, 47.
- [176] M. A. Sentef, M. Claassen, A. F. Kemper, B. Moritz, T. Oka, J. K. Freericks, T. P. Devereaux, *Nat. Commun.* **2015**, *6*, 7047.
- [177] B. M. Fregoso, Y. H. Wang, N. Gedik, V. Galitski, *Phys. Rev. B* **2013**, *88*, 155129.
- [178] M. Schüler, M. A. Sentef, *J. Electron Spectrosc. Relat. Phenom.* **2021**, *253*, 147121.
- [179] M. S. Rudner, N. H. Lindner, *ArXiv2003.08252*, **2020**.
- [180] J. K. Freericks, H. R. Krishnamurthy, Th. Pruschke, *Phys. Rev. Lett.* **2009**, *102*, 136401.
- [181] J. K. Freericks, H. R. Krishnamurthy, M. A. Sentef, T. P. Devereaux, *Phys. Scr.* **2015**, *T165*, 014012.
- [182] P. X. Nguyen, W.-K. Tse, *Phys. Rev. B* **2021**, *103*, 125420.
- [183] M. Ezawa, *Phys. Rev. Lett.* **2013**, *110*, 026603.
- [184] H. Liu, J.-T. Sun, C. Cheng, F. Liu, S. Meng, *Phys. Rev. Lett.* **2018**, *120*, 237403.
- [185] C. Dutreix, E. A. Stepanov, M. I. Katsnelson, *Phys. Rev. B* **2016**, *93*, 241404.
- [186] W. Yao, A. H. MacDonald, Q. Niu, *Phys. Rev. Lett.* **2007**, *99*, 047401.
- [187] M. Claassen, C. Jia, B. Moritz, T. P. Devereaux, *Nat. Commun.* **2016**, *7*, 13074.
- [188] T. Kitagawa, E. Berg, M. Rudner, E. Demler, *Phys. Rev. B* **2010**, *82*, 235114.
- [189] M. König, S. Wiedmann, C. Brüne, A. Roth, H. Buhmann, L. W. Molenkamp, X.-L. Qi, S.-C. Zhang, *Science* **2007**, *318*, 766.
- [190] N. Nagaosa, J. Sinova, S. Onoda, A. H. MacDonald, N. P. Ong, *Rev. Mod. Phys.* **2010**, *82*, 1539.
- [191] S. Murakami, N. Nagaosa, S.-C. Zhang, *Science* **2003**, *301*, 1348.
- [192] S. Aeschlimann, S. A. Sato, R. Krause, M. Chávez-Cervantes, U. De Giovannini, H. Hübener, S. Forti, C. Coletti, K. Hanff, K. Rossnagel, A. Rubio, I. Gierz, *Nano Lett.* **2021**, *21*, 5028.
- [193] A. Eckardt, E. Anisimovas, *New J. Phys.* **2015**, *17*, 093039.
- [194] G. Usaj, P. M. Perez-Piskunow, L. E. F. Foa Torres, C. A. Balseiro, *Phys. Rev. B* **2014**, *90*, 115423.
- [195] P. M. Perez-Piskunow, G. Usaj, C. A. Balseiro, L. E. F. F. Torres, *Phys. Rev. B* **2014**, *89*, 121401.
- [196] Y. Hatsugai, *Phys. Rev. Lett.* **1993**, *71*, 3697.
- [197] L. E. F. Foa Torres, P. M. Perez-Piskunow, C. A. Balseiro, G. Usaj, *Phys. Rev. Lett.* **2014**, *113*, 266801.
- [198] Z. Gu, H. A. Fertig, D. P. Arovas, A. Auerbach, *Phys. Rev. Lett.* **2011**, *107*, 216601.
- [199] A. Farrell, T. Pereg-Barnea, *Phys. Rev. Lett.* **2015**, *115*, 106403.
- [200] A. Farrell, T. Pereg-Barnea, *Phys. Rev. B* **2016**, *93*, 045121.
- [201] I. Esin, M. S. Rudner, G. Refael, N. H. Lindner, *Phys. Rev. B* **2018**, *97*, 245401.
- [202] H. Deghani, T. Oka, A. Mitra, *Phys. Rev. B* **2015**, *91*, 155422.
- [203] S. A. Sato, J. W. McClver, M. Nuske, P. Tang, G. Jotzu, B. Schulte, H. Hübener, U. De Giovannini, L. Mathey, M. A. Sentef, A. Cavalleri, A. Rubio, *Phys. Rev. B* **2019**, *99*, 214302.
- [204] M. Nuske, L. Broers, B. Schulte, G. Jotzu, S. A. Sato, A. Cavalleri, A. Rubio, J. W. McClver, L. Mathey, *Phys. Rev. Res.* **2020**, *2*, 043408.
- [205] S. A. Sato, P. Tang, M. A. Sentef, U. De Giovannini, H. Hübener, A. Rubio, *New J. Phys.* **2019**, *21*, 093005.
- [206] M. Schüler, U. De Giovannini, H. Hübener, A. Rubio, M. A. Sentef, T. P. Devereaux, P. Werner, *Phys. Rev. X* **2020**, *10*, 041013.
- [207] M. Schüler, S. Beaulieu, *Comms. Phys.* **2022**, *5*, 164.
- [208] J. Maklar, R. Stühler, M. Dendzik, T. Pincelli, S. Dong, S. Beaulieu, A. Neef, G. Li, M. Wolf, R. Ernstorfer, R. Claessen, L. Rettig, (*Preprint*), *ArXiv2108.09218* (submitted, Aug. 2021).
- [209] D. Fausti, R. I. Tobey, N. Dean, S. Kaiser, A. Dienst, M. C. Hoffmann, S. Pyon, T. Takayama, H. Takagi, A. Cavalleri, *Science* **2011**, *331*, 189.
- [210] S. W. Teitelbaum, T. Shin, J. W. Wolfson, Y.-H. Cheng, I. J. Porter, M. Kandyla, K. A. Nelson, *Phys. Rev. X* **2018**, *8*, 031081.
- [211] M. Mitrano, A. Cantaluppi, D. Nicoletti, S. Kaiser, A. Perucchi, S. Lupi, P. Di Pietro, D. Pontiroli, M. Riccò, S. R. Clark, D. Jaksch, A. Cavalleri, *Nature* **2016**, *530*, 461.
- [212] M. Budden, T. Gebert, M. Buzzi, G. Jotzu, E. Wang, T. Matsuyama, G. Meier, Y. Laplace, D. Pontiroli, M. Riccò, F. Schlawin, D. Jaksch, A. Cavalleri, *Nat. Phys.* **2021**, *17*, 611.
- [213] D. Nicoletti, E. Casandruc, Y. Laplace, V. Khanna, C. R. Hunt, S. Kaiser, S. S. Dhesi, G. D. Gu, J. P. Hill, A. Cavalleri, *Phys. Rev. B* **2014**, *90*, 100503.
- [214] K. A. Cremin, J. Zhang, C. C. Homes, G. D. Gu, Z. Sun, M. M. Fogler, A. J. Millis, D. N. Basov, R. D. Averitt, *Proc. Natl. Acad. Sci.* **2019**, *116*, 19875.
- [215] S. Carr, D. Massatt, S. Fang, P. Cazeaux, M. Luskin, E. Kaxiras, *Phys. Rev. B* **2017**, *95*, 075420.
- [216] E. Y. Andrei, A. H. MacDonald, *Nat. Mater.* **2020**, *19*, 1265.
- [217] S. Carr, S. Fang, E. Kaxiras, *Nat. Rev. Mater.* **2020**, *5*, 748.
- [218] M. Vogl, M. Rodriguez-Vega, G. A. Fiete, *Phys. Rev. B* **2020**, *101*, 235411.
- [219] O. Katz, G. Refael, N. H. Lindner, *Phys. Rev. B* **2020**, *102*, 155123.
- [220] G. E. Topp, G. Jotzu, J. W. McClver, L. Xian, A. Rubio, M. A. Sentef, *Phys. Rev. Res.* **2019**, *1*, 023031.
- [221] M. Vogl, M. Rodriguez-Vega, G. A. Fiete, *Phys. Rev. B* **2020**, *101*, 241408.
- [222] V. M. Galitskii, S. P. Goreslavskii, V. F. Elesin, *J. Theor. Exp. Phys.* **1970**, *30*, 117.
- [223] L. I. Glazman, *J. Theor. Exp. Phys.* **1981**, *53*, 178.
- [224] L. D'Alessio, M. Rigol, *Phys. Rev. X* **2014**, *4*, 041048.
- [225] A. Lazarides, A. Das, R. Moessner, *Phys. Rev. E* **2014**, *90*, 012110.
- [226] D. Abanin, W. De Roeck, W. W. Ho, F. Huveneers, *Commun. Math. Phys.* **2017**, *354*, 809.
- [227] O. Howell, P. Weinberg, D. Sels, A. Polkovnikov, M. Bukov, *Phys. Rev. Lett.* **2019**, *122*, 010602.
- [228] M. Vogl, P. Laurell, A. D. Barr, G. A. Fiete, *Phys. Rev. X* **2019**, *9*, 021037.
- [229] K. Singh, C. J. Fujiwara, Z. A. Geiger, E. Q. Simmons, M. Lipatov, A. Cao, P. Dotti, S. V. Rajagopal, R. Senaratne, T. Shimasaki, M. Heyl, A. Eckardt, D. M. Weld, *Phys. Rev. X* **2019**, *9*, 041021.
- [230] D. A. Abanin, W. De Roeck, F. Huveneers, *Phys. Rev. Lett.* **2015**, *115*, 256803.
- [231] M. Bukov, L. D'Alessio, A. Polkovnikov, *Adv. Phys.* **2015**, *64*, 139.
- [232] T. Kuwahara, T. Mori, K. Saito, *Ann. Phys.* **2016**, *367*, 96.
- [233] K. I. Seetharam, C.-E. Bardyn, N. H. Lindner, M. S. Rudner, G. Refael, *Phys. Rev. B* **2019**, *99*, 014307.
- [234] K. I. Seetharam, C.-E. Bardyn, N. H. Lindner, M. S. Rudner, G. Refael, *Phys. Rev. X* **2015**, *5*, 041050.
- [235] T. Iadecola, T. Neupert, C. Chamon, *Phys. Rev. B* **2015**, *91*, 235133.
- [236] H. Deghani, T. Oka, A. Mitra, *Phys. Rev. B* **2014**, *90*, 195429.
- [237] M. Genske, A. Rosch, *Phys. Rev. A* **2015**, *92*, 062108.
- [238] I. Esin, G. K. Gupta, E. Berg, M. S. Rudner, N. H. Lindner, *Nat. Commun.* **2021**, *12*, 5299.
- [239] I. Esin, M. S. Rudner, N. H. Lindner, *Sci. Adv.* **2020**, *6*, eaay4922.
- [240] D. Curcio, S. Pakdel, K. Volckaert, J. A. Miwa, S. Ulstrup, N. Lanatà, M. Bianchi, D. Kutnyakhov, F. Pressacco, G. Brenner, S. Dziarzhyski, H. Redlin, S. Y. Agustsson, K. Medjanik, D. Vasilyev, H.-J. Elmers, G. Schönhense, C. Tusche, Y.-J. Chen, F. Speck, T. Seyller, K. Bühlmann, R. Gort, F. Diekmann, K. Rossnagel, Y. Acremann, J. Demsar, W. Wurth, D. Lizzit, L. Bignardi, et al., *Phys. Rev. B* **2021**, *104*, L161104.
- [241] X. Huang, T. Wang, S. Miao, C. Wang, Z. Li, Z. Lian, T. Taniguchi, K. Watanabe, S. Okamoto, D. Xiao, S.-F. Shi, Y.-T. Cui, *Nat. Phys.* **2021**, *17*, 715.

- [242] P. V. Nguyen, N. C. Teutsch, N. P. Wilson, J. Kahn, X. Xia, A. J. Graham, V. Kandyba, A. Giampietri, A. Barinov, G. C. Constantinescu, N. Yeung, N. D. M. Hine, X. Xu, D. H. Cobden, N. R. Wilson, *Nature* **2019**, 572, 220.
- [243] G. Schönhense, D. Kutnyakhov, F. Pressacco, M. Heber, N. Wind, S. Y. Agustsson, S. Babenkov, D. Vasilyev, O. Fedchenko, S. Chernov, L. Rettig, B. Schönhense, L. Wenthaus, G. Brenner, S. Dziarzhytski, S. Palutke, S. K. Mahatha, N. Schirmel, H. Redlin, B. Manschwetus, I. Hartl, Y. Matveyev, A. Gloskovskii, C. Schlueter, V. Shokeen, H. Durr, T. K. Allison, M. Beye, K. Rossnagel, H. J. Elmers, et al., *Rev. Sci. Instrum.* **2021**, 92, 053703.



Ouri Karni is a research scientist in the Department of Applied Physics, Stanford University, working with Prof. Tony F. Heinz. His main area of research is the optical properties of 2D materials and the spectroscopy of their excited states. His Ph.D. in Electrical Engineering is from the Technion—Israel Institute of Technology studying the dynamics of nano-structured semiconducting optical gain media and lasers. He holds a B.Sc. degree in Electrical Engineering and a BA in Physics from the Technion—Israel Institute of Technology.



Iliya Esin is a postdoctoral scholar research associate in Theoretical Physics, in the Division of Physics, Mathematics, and Astronomy, at Caltech—California Institute of Technology. His main research interests are in the fields of low-dimensional quantum materials, light–matter interactions, topological phases of matter, and out-of-equilibrium many-body dynamics. He holds a Ph.D. degree in Physics from the Technion—Israel Institute of Technology, an M.Sc. degree in Physics from the Weizmann Institute of Science, a B.Sc. degree in Physics, and a B.Sc. degree in Electrical Engineering from Tel Aviv University.



Keshav M. Dani is an associate professor at the Okinawa Institute of Science and Technology (OIST), Graduate University in Okinawa, Japan. He joined OIST in 2011 after a Director's Postdoctoral Fellowship at Los Alamos National Laboratory. His Ph.D. research in Physics (UC Berkeley), supervised by Prof. Daniel Chemla, explored the nonlinear optical response of the quantum Hall system. He obtained a B.Sc. from Caltech in Mathematics with a senior thesis in Quantum Information Theory under John Preskill and Hideo Mabuchi. His current research uses time-resolved multi-dimensional photoemission techniques to study electron dynamics of 2D materials and energy materials.